Revealing the intrinsic oxygen evolution reaction activity of perovskite oxides across conductivity ranges using thin film model systems

Lisa Heymann[†,*], Iris C. G. van den Bosch[§], Daan Wielens[§], Ole Kurbjeweit[†], Emma van der Minne[§], Ellen M. Kiens[§], Anton Kaus[†], Daniel Schön[†], Stephan Menzel[†], Bernard Boukamp[§], Felix Gunkel[†,*], Christoph Baeumer[†,§,*]

[†]Peter Gruenberg Institute 7, Forschungszentrum Juelich GmbH, 52428 Juelich, Germany and JARA-FIT, RWTH Aachen University, 52056 Aachen, Germany

[§]MESA+ Institute for Nanotechnology, Faculty of Science and Technology, University of Twente, Enschede, Netherlands

*Corresponding authors

Abstract:

The development of efficient electrocatalysts in water electrolysis is essential to decrease the high overpotentials especially at the anode where the oxygen evolution reaction (OER) takes place. However, establishing catalyst design rules to find optimal electrocatalysts is a substantial challenge. Complex oxides, which are often considered as suitable OER catalysts, can exhibit vastly different conductivity values, making it challenging to separate intrinsic catalytic activities from internal transport limitations. Here, we systematically decouple the limitations arising from electrical bulk resistivity, contact resistances to the catalyst support, and intrinsic OER catalytic properties using a systematic epitaxial thin film model catalyst approach. We investigate the influence of the resistivity of the three perovskite oxides $LaNiO_{3-\delta}$ ($3.7x10^{-4}$ Ωcm), $La_{0.67}Sr_{0.33}MnO_{3-\delta}$ ($2.7x10^{-3}$ Ωcm) and $La_{0.6}Ca_{0.4}FeO_{3-\delta}$, (0.57 Ωcm) on the observed catalytic activity. We tune the electron pathway through the catalyst bulk by comparing insulating and conductive substrates. The conducting substrate reduces the electron pathway through the catalyst bulk from millimeter to nanometer length scale. As we show, for the large electron pathways, the observed catalytic activity scales with the resistivity because of a highly inhomogeneous lateral current density distribution. At the same time, even on the conducting substrate (Nb-doped $SrTiO_3$), large contact resistances occur that limit the determination of intrinsic catalytic properties. By inserting interfacial dipole layers (in this case $LaAlO_3$) we lifted these interface resistances, allowing us to reveal the intrinsic catalytic properties of all examined catalysts. We find that $La_{0.6}Ca_{0.4}FeO_{3-\delta}$ and $LaNiO_{3-\delta}$ exhibit a similar intrinsic overpotential of 0.36 V at 0.1 mA/cm^2, while their resistivities differ by three orders of magnitude. This finding shows that optimizing the electron pathway of OER catalyst can lead the way to find new structure-activity relationships and to identify high-activity catalysts even if the electronic resistance is high.

Keywords: electrocatalysis, oxygen evolution reaction, conductivity, resistivity, perovskite oxide, interface layer, intrinsic catalytic activity

Introduction

Electrochemical energy conversion technologies such as electrolyzers or fuel cells are crucial for renewable energy storage, e-fuel synthesis, and a non-fossil-based industry[1,2]. One prominent example is a water electrolyzer where hydrogen is produced on the cathode via the hydrogen evolution reaction and oxygen is produced on the anode via the oxygen evolution reaction (OER). The optimization of catalytic processes taking place at the interface between catalyst and the electrolyte remain a challenge, particularly for the OER as it suffers from sluggish kinetics, that limit the efficiency of the overall reaction[3,4]. Therefore, the catalytic properties of the OER catalyst material must be optimized to decrease the OER overpotential[3,4]. Perovskite oxides are one promising material class to reduce the high overpotentials in the OER. They exhibit an ABO_3 structure where the A-site is typically occupied by rare earth elements and alkaline earth elements, and the B-site is occupied with transition metals[5]. However, the electrical conductivity of perovskites varies by orders of magnitude, depending on the B-site transition metal doping level and/or the defect structure of the material[6–8]. In the literature, it is often addressed that a high electrical conductivity, ensuring an unhindered electron pathway through the material bulk, is a crucial necessity for a good electrocatalyst[9]. Therefore, perovskites with high resistivity are often described to be poor electrocatalysts such as $LaFeO_3$, $LaCoO_3$ or $LaMnO_3$ [10,11], and low-conductivity perovskites have been discarded from catalyst research in some cases, due to the difficulty to run sufficiently high current[12]. However, it is hard to disentangle whether low electrochemical activity stems from high bulk resistivity or poor intrinsic catalytic properties[13,14]. The intrinsic catalytic properties reflect the ability to lower the kinetic barriers for the electrochemical reaction at the electrolyte/catalyst interface, independent of their resistivity and additional stack resistances. For example, substituting Ni into the solid-solution series of $La_{0.7}Sr_{0.3}Fe_{1-x}Ni_xO_{3-\delta}$ induces a phase transition and increased oxygen vacancy content leading to an overall lower resistivity that correlates with the OER performance[15]. Furthermore, $LaCoO_3$ shows comparably low OER activity in experiment, but lowering its resistivity through compressive lattice strain and introducing conductive support layers increases the OER activity[16,17]. Additionally, contact resistances (induced e.g. through space charge layers) at the interface to the substrate or support layer can dilute the determination

of intrinsic catalytic properties[18–22]. These examples indicate a correlation between electrical and electrochemical properties, yet it remains often unclear if a varied electrical resistivity directly affects the intrinsic catalytic activity of the OER catalyst. Further, the relations between electron transport pathways, bulk and interface resistances remain unclear and pathway-dependent current density losses are not quantified.

In this paper, we systematically decouple the intrinsic catalytic properties from bulk resistivity for perovskite oxides, covering a resistivity range of three orders of magnitude. We employ an epitaxial thin film model system approach to tune the electron transport pathway through the catalyst bulk and thin film stack. Single crystalline epitaxial thin films of perovskite oxides principally give the opportunity to reveal intrinsic properties[23–25]. These model catalysts are free of catalyst binder and conductive carbon, and exhibit smooth surface morphologies with single crystal facet orientation, allowing to determine catalytic properties also free of grain boundary effects[23,25,26].

Here, we choose the three perovskite oxides $LaNiO_{3-\delta}$, $La_{0.67}Sr_{0.33}MnO_{3-\delta}$ and $La_{0.6}Ca_{0.4}FeO_{3-\delta}$ as epitaxial thin films in (001) orientation, exhibiting the resistivities of $3.7x10^{-4}$ Ωcm, $2.7x10^{-3}$ Ωcm and 0.57 Ωcm, respectively. When the thin films are deposited on insulating substrates, the electron transport pathway through the bulk is several millimeters long, and the observed OER activity follows the trend of the resistivities of the three perovskite oxides. To quantify inhomogeneous current density distributions, we conduct a COMSOL study, where the highly resistive $La_{0.6}Ca_{0.4}FeO_{3-\delta}$ shows tremendous current density variations along the catalyst/electrolyte interface. Switching to conducting Nb-doped $SrTiO_3$ substrates decreases the electron transport pathway to nanometer length scales. However, large contact resistances occur between the substrate and thin films as also reported elsewhere[22,27]. Decreasing the contact resistance via interface engineering finally allows us to reveal the intrinsic catalytic properties of the three perovskites. Surprisingly, the initially inactive and highly resistive $La_{0.6}Ca_{0.4}FeO_{3-\delta}$ thin film shows similarly high intrinsic OER activity as the metallic $LaNiO_{3-\delta}$, and $La_{0.67}Sr_{0.33}MnO_{3-\delta}$ shows the lowest intrinsic OER activity. The results show that the intrinsic catalytic activity of electrocatalysts across large conductivity ranges can be determined when appropriate and individualized sample design is applied.

Results

10-25 nm thick epitaxial thin films of $LaNiO_{3-\delta}$, $La_{0.67}Sr_{0.33}MnO_{3-\delta}$ and $La_{0.6}Ca_{0.4}FeO_{3-\delta}$ were grown by pulsed laser deposition (PLD) on single crystal (100) $SrTiO_3$ substrates. The growth was tracked by reflection high energy electron diffraction (RHEED) enabling us to control the desired thin film thickness on single unit cell level. Figure S1 of the supporting information (SI) shows representative RHEED data, x-ray diffraction (XRD) and atomic force microscopy, confirming the well-defined synthesis of the OER model catalysts. To determine the electrical resistivity (ρ), the sheet resistance was measured in van der Pauw geometry. The resistivity of $LaNiO_{3-\delta}$ is $3.7x10^{-4}$ Ωcm (**Figure 1a**) followed by $La_{0.67}Sr_{0.33}MnO_{3-\delta}$ with one order of magnitude higher resistivity ($2.7x10^{-3}$ Ωcm) and finally $La_{0.6}Ca_{0.4}FeO_{3-\delta}$ with three orders of magnitude higher resistivity (0.57 Ωcm). The resistivity values of $LaNiO_{3-\delta}$ and $La_{0.67}Sr_{0.33}MnO_{3-\delta}$ grown $SrTiO_3$ on are consistent with the literature[28–30]. For $La_{0.6}Ca_{0.4}FeO_{3-\delta}$ powder, a resistivity of 29 Ωcm was reported[31].

Electrochemical measurements were conducted in a three-electrode configuration, with a rotating disc electrode (RDE). The thin film samples were mounted on the RDE shaft as illustrated in Figure S2a, using the same approach as reported previously[32]. For thin films deposited on insulating $SrTiO_3$ substrates, Pt was sputtered on the sample backside, edges, and frontside edges (see sketch in SI Figure S2b and Figure 1b), to provide current collection from the sides of the thin film electrocatalysts.

The OER activity of $LaNiO_{3-\delta}$, $La_{0.67}Sr_{0.33}MnO_{3-\delta}$ and $La_{0.6}Ca_{0.4}FeO_{3-\delta}$ was assessed using cyclic voltammetry (CV, **Figure 1b**). The CV scans were *iR* corrected with the uncompensated resistance (R_u) obtained from open circuit voltage (OCV) impedance spectroscopy (**Figure 1c**). The current density was determined for the geometric surface area which is the area of the inner O-ring diameter. The $LaNiO_{3-\delta}$ thin film shows the highest OER activity with an overpotential ($\eta = E_{OER} - 1.23\ V$) of 0.37 V at 0.1 mA/cm^2 followed by $La_{0.67}Sr_{0.33}MnO_{3-\delta}$ with η = 0.44 V. The $La_{0.6}Ca_{0.4}FeO_{3-\delta}$ thin film shows the lowest OER activity with an overpotential of 0.53 V at 0.1 mA/cm^2. The observed OER activity is hence scaling with the resistivity of $LaNiO_{3-\delta}$, $La_{0.67}Sr_{0.33}MnO_{3-\delta}$ and $La_{0.6}Ca_{0.4}FeO_{3-\delta}$.

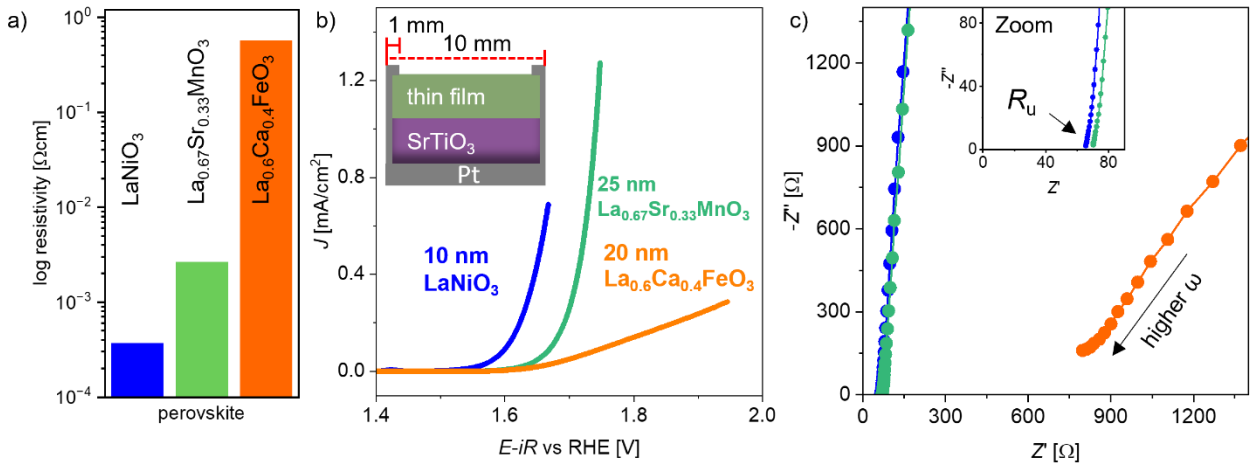

Figure 1: a) Resistivity of $LaNiO_{3-\delta}$, $La_{0.67}Sr_{0.33}MnO_{3-\delta}$ and $La_{0.6}Ca_{0.4}FeO_{3-\delta}$. b) Cyclic voltammetry scans of $LaNiO_{3-\delta}$, $La_{0.67}Sr_{0.33}MnO_{3-\delta}$ and $La_{0.6}Ca_{0.4}FeO_{3-\delta}$ on $SrTiO_3$, with Pt side contacts to the back. The CV data is iR corrected and averaged between anodic and cathodic sweep from the second CV cycle. c) Nyquist plots in the high frequency (ω) range of $LaNiO_{3-\delta}$, $La_{0.67}Sr_{0.33}MnO_{3-\delta}$ and $La_{0.6}Ca_{0.4}FeO_{3-\delta}$ measured at open circuit voltage (graph colors correspond to the legend in b)). The inset shows a zoom of the Nyquist plot to the high frequency intercept of $LaNiO_{3-\delta}$ and $La_{0.67}Sr_{0.33}MnO_{3-\delta}$.

The CV scan of the $La_{0.6}Ca_{0.4}FeO_{3-\delta}$ sample exhibits a close-to linear slope at higher current densities, suggesting that an ohmic resistance suppresses the typically expected exponential behavior. This hints at a current limitation caused by the high bulk resistivity of $La_{0.6}Ca_{0.4}FeO_{3-\delta}$, rather than to a limitation caused by its intrinsic catalytic activity. The presence of an additional ohmic resistance in addition to the electrolyte resistance is also apparent in the electrochemical impedance data (**Figure 1c**). The R_u of $LaNiO_{3-\delta}$ and $La_{0.67}Sr_{0.33}MnO_{3-\delta}$ are 65 Ω and 70 Ω (cf. inset in **Figure 1c**), while the R_u of $La_{0.6}Ca_{0.4}FeO_{3-\delta}$ is about an order of magnitude higher (724 Ω). Further, the imaginary part of the impedance, -*Z*'', shows a larger offset from the abscissa. This occurs because the catalyst impedance signal overlaps with the impedance signal caused by the reference electrode (see SI Figure S3 for a detailed discussion)[22,33]. Although the OER CV scan of $La_{0.6}Ca_{0.4}FeO_{3-\delta}$ (**Figure 1b**) was *iR* corrected with the R_u of 724 Ω, this *iR* correction appears to be insufficient to eliminate all ohmic resistances. A possible reason might be that the employed fitting procedure to determine R_u underestimates the true serial resistances in the cell, e.g., due to the large offset from the abscissa. Alternatively, the *x*-axis offset as measured in impedance spectroscopy might not include all bulk related resistances, a point to which we will return below. Note

that typical R_u values are between 40 Ω and 60 Ω in 0.1 M KOH with Pt electrodes in this cell geometry (see SI Figure S3a), indicating that our measured R_u values contain a small contribution from sample-specific resistance (for $LaNiO_{3-\delta}$ and $La_{0.67}Sr_{0.33}MnO_{3-\delta}$), or are dominated by sample resistance, as is the case for $La_{0.6}Ca_{0.4}FeO_{3-\delta}$.

The observed scaling with resistivity may be rationalized by the sample geometry. The chosen side-contacting implies that electrons released in redox reactions at the center of the 10x10 mm^2 sample must travel up to 4 mm through the bulk of the catalyst layer to reach the metal contact (Figure S2b). The comparably high resistivity of $La_{0.6}Ca_{0.4}FeO_{3-\delta}$ suppresses the electron transport from the reaction site at the solid-liquid interface to the metallic contacts to a larger extent than is the case for $LaNiO_{3-\delta}$ and $La_{0.67}Sr_{0.33}MnO_{3-\delta}$. Hence, the thin film resistivity might play a significant role for the measured OER activities.

To investigate this possible electron transport limitation in the thin film towards the metallic side contact independent of the sluggish OER kinetics, we employed CV in hexacyano ferrate $K_4[Fe(CN)_6]/K_3[Fe(CN)_6]$ containing electrolyte, constituting the outer-sphere reversible redox couple Fe^{2+}/Fe^{3+} (in the following denoted as Fe^{2+}/Fe^{3+}). To obtain the typical duck shape of the CV scan, the rotation is turned off for this experiment. In contrast to inner-sphere electrocatalytic reactions like the OER, such outer-sphere fast redox couples have no significant material-dependent kinetic charge-transfer challenges but can directly reveal electronic transport limitations. For barrier-free band alignment at all involved interfaces and a low overall resistance, one expects a reversible redox process with symmetric anodic and cathodic peaks and a small peak potential separation. Any decrease in peak height as well as asymmetries can be related towards electronic resistances in the electrode stack[24] (or in some cases toward smaller surface areas[34]). The redox potential of Fe^{2+} to Fe^{3+} is 1.2 V vs. RHE, which is similar to the theoretical OER redox potential, giving the advantage to test electron transport limitations in the relevant potential range[24].

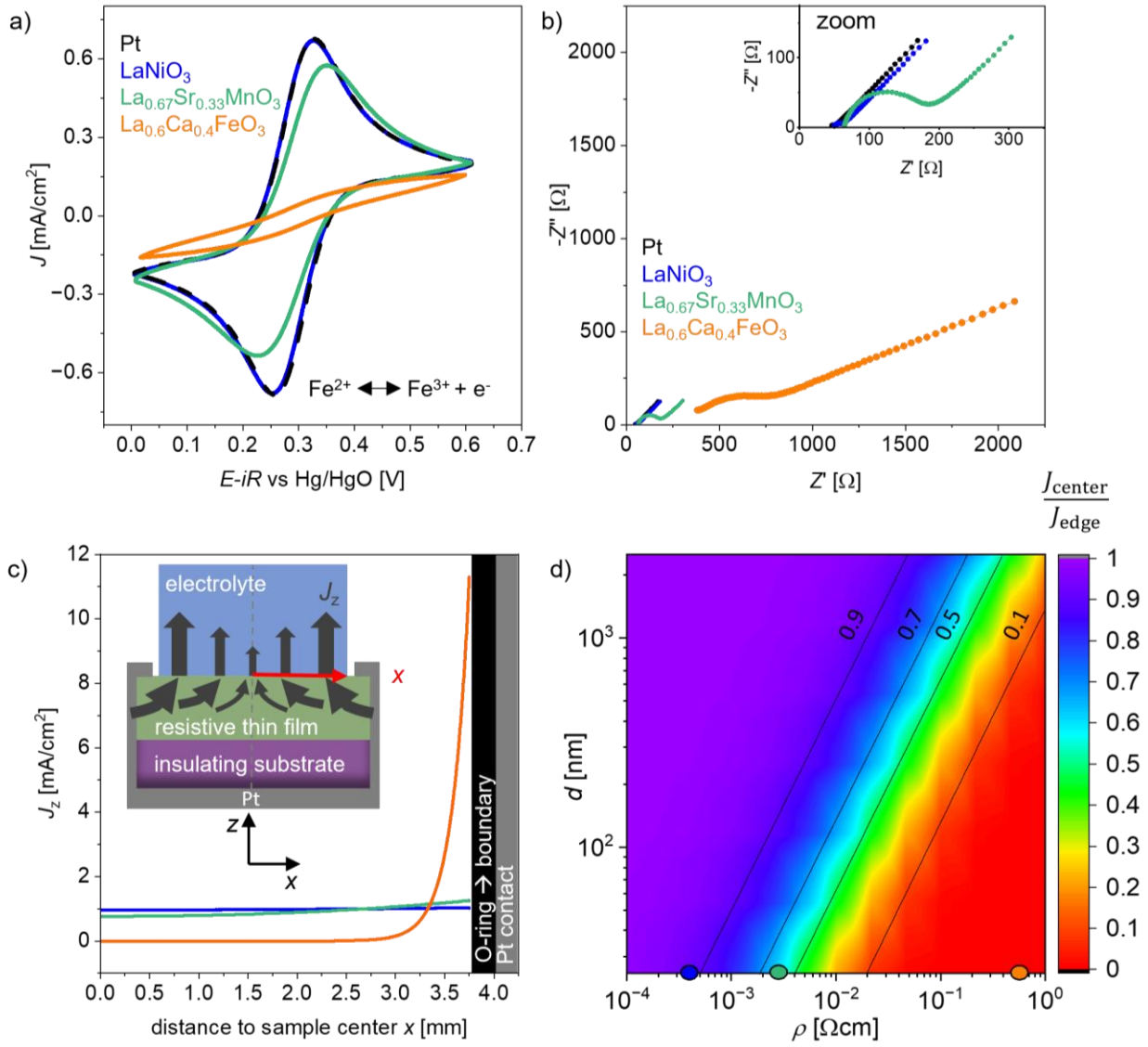

Figure 2: a). Cyclic voltammetry scans of $LaNiO_{3-\delta}$, $La_{0.67}Sr_{0.33}MnO_{3-\delta}$ and $La_{0.6}Ca_{0.4}FeO_{3-\delta}$ in $K_4[Fe(CN)_6]/K_3[Fe(CN)_6]$ solution. b) Corresponding impedance spectroscopy measured at OCV. The inset shows a zoom to the region of 350 Ω in Z' direction. c) Simulated current density distribution of the thin films on insulating substrates. The inset shows a sketch of the radial current density distribution $J_z(x)$ on resistive thin films along the x axis of the simulation. The dashed line in the center represents the axisymmetric line cut. d) Heat map of the current density variation $\frac{J_{center}}{J_{edge}}$ as a function of catalyst layer resistivity ρ and thickness d. Blue, green and orange dots are the data points for 25 nm thick $LaNiO_{3-\delta}$, $La_{0.67}Sr_{0.33}MnO_{3-\delta}$ and $La_{0.6}Ca_{0.4}FeO_{3-\delta}$ thin films, respectively.

We compared the Fe^{2+}/Fe^{3+} CV scans of 25 nm thick $LaNiO_{3-\delta}$, $La_{0.67}Sr_{0.33}MnO_{3-\delta}$ and $La_{0.6}Ca_{0.4}FeO_{3-\delta}$ thin films to a Pt thin film acting as an ideally metallic reference (**Figure 2a**). $LaNiO_{3-\delta}$ and Pt exhibit strongly

overlapping CV curves, indicating that the electron transport to the side contacts of the $LaNiO_{3-\delta}$ thin film is not limiting and the redox reaction exhibits no significant overpotential for $LaNiO_{3-\delta}$. $La_{0.67}Sr_{0.33}MnO_{3-\delta}$ shows a slightly increased overpotential for the oxidation and reduction of Fe^{2+}/Fe^{3+}, as indicated by the slight decrease and shift of the current density maximum towards higher and lower potentials, respectively. In contrast, $La_{0.6}Ca_{0.4}FeO_{3-\delta}$ exhibits no clear oxidation and reduction peaks in this potential range, indicating that its high resistivity strongly limits the electron transport.

As can be seen in **Figure 2b**, the corresponding impedance spectra recorded at OCV in Fe^{2+}/Fe^{3+} containing electrolyte show a similar behavior. $LaNiO_{3-\delta}$ and Pt exhibit comparable spectra whereas $La_{0.67}Sr_{0.33}MnO_{3-\delta}$ exhibits a larger semi-circle in the high frequency range. In the low frequency range, the impedance shows a nearly linear increase at an angle close to 45° for the Pt, $LaNiO_{3-\delta}$ and $La_{0.67}Sr_{0.33}MnO_{3-\delta}$ thin films, indicating the presence of a semi-infinite Warburg element[35] in the equivalent circuit. This feature stems from the mass transport limitations of the Fe^{2+}/ Fe^{3+} species at the solid/liquid interface. The slight overpotentials observed for $La_{0.67}Sr_{0.33}MnO_{3-\delta}$ in the CV scan in Figure 2a could stem from a higher resistivity compared to $LaNiO_{3-\delta}$, but the observed semi-circle in the impedance indicates that there could be a significant interface barrier for the $La_{0.67}Sr_{0.33}MnO_{3-\delta}$ thin film reducing the observed currents as well. For $La_{0.6}Ca_{0.4}FeO_{3-\delta}$, R_u exhibits a significantly higher value since the higher total resistance of the thin film might add up to the overall observed *x*-axis offset, similar to the behavior of the impedance shown in Figure 1c. Moreover, the observed semi-circle in the high frequency range is deformed, a characteristic often represented by a constant phase element in equivalent electrical circuits. The low-frequency region shows a distorted incline with a slope less than 45°, which indicates that the condition for an ideal Warburg element is not fulfilled either. Together, the CV and impedance spectroscopy with the Fe^{2+}/ Fe^{3+} redox couple confirm that thin films with a high resistivity exhibit poor electrochemical performance due to impeded electron transport in the film.

To investigate and quantify the influence of the thin film resistivity on the local current density along the thin film/electrolyte interface, a COMSOL Multiphysics study was conducted for the $LaNiO_{3-\delta}$, $La_{0.67}Sr_{0.33}MnO_{3-\delta}$ and $La_{0.6}Ca_{0.4}FeO_{3-\delta}$ films which is illustrated in **Figure 2c**. In the COMSOL simulation, a

fixed current of 0.44 mA was applied corresponding to an average current density of 1 mA/cm^2 as the exposed geometric surface area is 0.44 cm^2. We simulated the current density distribution $J_z(x)$ across the catalyst surface from the sample center to the boundary of the catalyst, i.e. the location of the O-ring at 3.75 mm distance from the sample center. The metallic contacts are located in 4 mm distance to the sample center, approximating the real sample geometry in the RDE setup. $J_z(x)$ is the current density perpendicular to the catalyst surface, read out along the sample interface in x direction (further details of the simulation can be found in the methods section and in the SI Figure S4).

The resulting current density distribution shows significant differences for the three materials with varying resistivities. For $LaNiO_{3-\delta}$, the current density is almost homogeneously distributed, indicating that the low resistivity does not significantly affect the current pathway through the thin film towards the metallic contacts, and the entire catalyst area contributes similarly to the reaction current. In the sample center, the current density is 0.96 mA/cm^2 and increases to 1.04 mA/ cm^2 at the catalyst boundary. To describe the current density variation along the sample profile, we define the ratio $\frac{J_{\mathrm{center}}}{J_{\mathrm{edge}}}$ which is the current density at the sample center in relation to the catalyst boundary:

$$\frac{J_{\mathrm{center}}}{J_{\mathrm{edge}}} = \frac{J_{\mathrm{z}}(x{=}0\ \mathrm{mm})}{J_{\mathrm{z}}(x{=}3.75\ \mathrm{mm})}.$$

For $LaNiO_{3-\delta}$, $\frac{J_{\mathrm{center}}}{J_{\mathrm{edge}}}$ is about 0.92. For $La_{0.67}Sr_{0.33}MnO_{3-\delta}$, however, the current density in the sample center is only 0.76 mA/cm^2 which is ~20 % lower than the value obtained for $LaNiO_{3-\delta}$. The current density increases continuously from the sample center towards the catalyst boundary reaching a current density of around 1.25 mA/cm^2. Hence, the one order of magnitude higher resistivity in the $La_{0.67}Sr_{0.33}MnO_{3-\delta}$ film leads to a significant change of the current density distribution along the interface, where $\frac{J_{\mathrm{center}}}{J_{\mathrm{edge}}}$ is only 0.6. This behavior is even more pronounced for $La_{0.6}Ca_{0.4}FeO_{3-\delta}$. Here, the current density is only 3.6 nA/cm^2 in the sample center and essentially does not contribute to the overall reaction. At 3 mm radial distance, the current density increases to 0.15 mA/cm^2. And only towards the edge, the current density increases drastically to more than 11 mA/cm^2 leading to an extremely small $\frac{J_{\mathrm{center}}}{J_{\mathrm{edge}}}$ ratio of only 2 x 10^{-8}. Due to the high resistance of the $La_{0.6}Ca_{0.4}FeO_{3-\delta}$ thin film, the area close to the metal contacts hence over-

proportionally contributes to the current and shows a locally higher current density (as sketched in the inset of **Figure 2c**).

Hence, the COMSOL study shows that the effective surface area accessible for electrochemical reactions is extremely small for $La_{0.6}Ca_{0.4}FeO_{3-\delta}$ in the chosen sample geometry. Therefore, for samples with higher resistivity, the observed electrochemical currents can effectively not be related to their geometric surface area that is exposed to the electrolyte, making it impossible to reveal their intrinsic catalytic properties in any electrochemical reaction in such sample geometry. The observed low activity of $La_{0.6}Ca_{0.4}FeO_{3-\delta}$ (**Figure 1b**) thus results from ill-defined normalization of the current density with respect to the total exposed catalyst area.

To determine which resistivity-thickness relations are suitable to reveal the intrinsic properties for this sample geometry, we extended the COMSOL study for the full resistivity range from 10^{-4} Ωcm to 1 Ωcm and thin film thicknesses of up to 2.5 µm. The expected current density ratio $\frac{J_{\mathrm{center}}}{J_{\mathrm{edge}}}$ is determined for various combinations of catalyst resistivity and layer thickness, yielding the heat map shown in **Figure 2d.**The values for 25 nm thick $LaNiO_{3-\delta}$, $La_{0.67}Sr_{0.33}MnO_{3-\delta}$ and $La_{0.6}Ca_{0.4}FeO_{3-\delta}$ thin films are marked as blue, green and orange dot, respectively.

We consider the $LaNiO_{3-\delta}$ case with $\frac{J_{\mathrm{center}}}{J_{\mathrm{edge}}}$ = 0.92 as an acceptable scenario to extract intrinsic catalytic properties in this geometry, while for $La_{0.67}Sr_{0.33}MnO_{3-\delta}$ with $\frac{J_{\mathrm{center}}}{J_{\mathrm{edge}}}$ = 0.6 the current density would already be too inhomogeneous for a proper analysis. However, with an exemplary sample thickness of more than 200 nm, $\frac{J_{\mathrm{center}}}{J_{\mathrm{edge}}}$ would be 0.9 or more also for $La_{0.67}Sr_{0.33}MnO_{3-\delta}$, enabling us to principally reveal the intrinsic catalytic properties of $La_{0.67}Sr_{0.33}MnO_{3-\delta}$ in this sample geometry. For $La_{0.6}Ca_{0.4}FeO_{3-\delta}$, however, even a film thickness of 1 µm would only lead to $\frac{J_{\mathrm{center}}}{J_{\mathrm{edge}}}$ = 0.2, making it impossible to determine the intrinsic catalytic properties in this sample geometry. Figure S5 shows the heatmap on a logarithmic scale, highlighting the extremely small $\frac{J_{\mathrm{center}}}{J_{\mathrm{edge}}}$ values for resistivities above $2{\cdot}10^{-2}$ Ωcm.

We emphasize that even though the trends presented in **Figure 2e** will be valid for any geometrical setup, i.e. $\frac{J_{\mathrm{center}}}{J_{\mathrm{edge}}}$ increases with increasing film thickness or decreasing film resistivity, the absolute values of $\frac{J_{\mathrm{center}}}{J_{\mathrm{edge}}}$ depend also on the lateral geometry of the experimental setup. If the setup deviates greatly from the one used here, additional simulations would be required to accurately estimate the variation in the current density across the interface between the thin film and the electrolyte. Nevertheless, the heat map can be used as an qualitative guidance for any thin film geometry applied to OER catalysis.

The previously mentioned ill-defined normalization of the current density in $La_{0.6}Ca_{0.4}FeO_{3-\delta}$ can also explain the deformed impedance features observed in **Figure 2b**. As the current-potential distribution exhibits a strong radial distribution, the equivalent electric circuit needs to be described as a series of R_u-*RC* elements that vary along the solid/liquid interface. Such 2D surface distributions are experimentally observed as a constant phase element in the global impedance[36–38], thus explaining the suppressed impedance feature in the high and low frequency ranges observed for $La_{0.6}Ca_{0.4}FeO_{3-\delta}$. An additional reason for the non-ideal Warburg element in **Figure 2b** could be sideward diffusion of ionic species in the electrolyte, which has been observed as an edge effect[39] that can principally also occur on metallic electrodes. The phenomenon of varied radial current-potential distribution could also occur in the catalyst bulk where not solely ohmic resistances are present but also capacitive contributions[40,41] might be present in the lateral dimension. Hence, the catalyst bulk might also be described as 2D distributed RC elements along the lateral dimension. Therefore, R_u determined by the *x*-axis intercept of the impedance at high frequencies does not include all relevant bulk related impedances. This might explain the fact that the linear slope observed for $La_{0.6}Ca_{0.4}FeO_{3-\delta}$ in **Figure 1a** cannot be compensated by a classic iR_u correction.

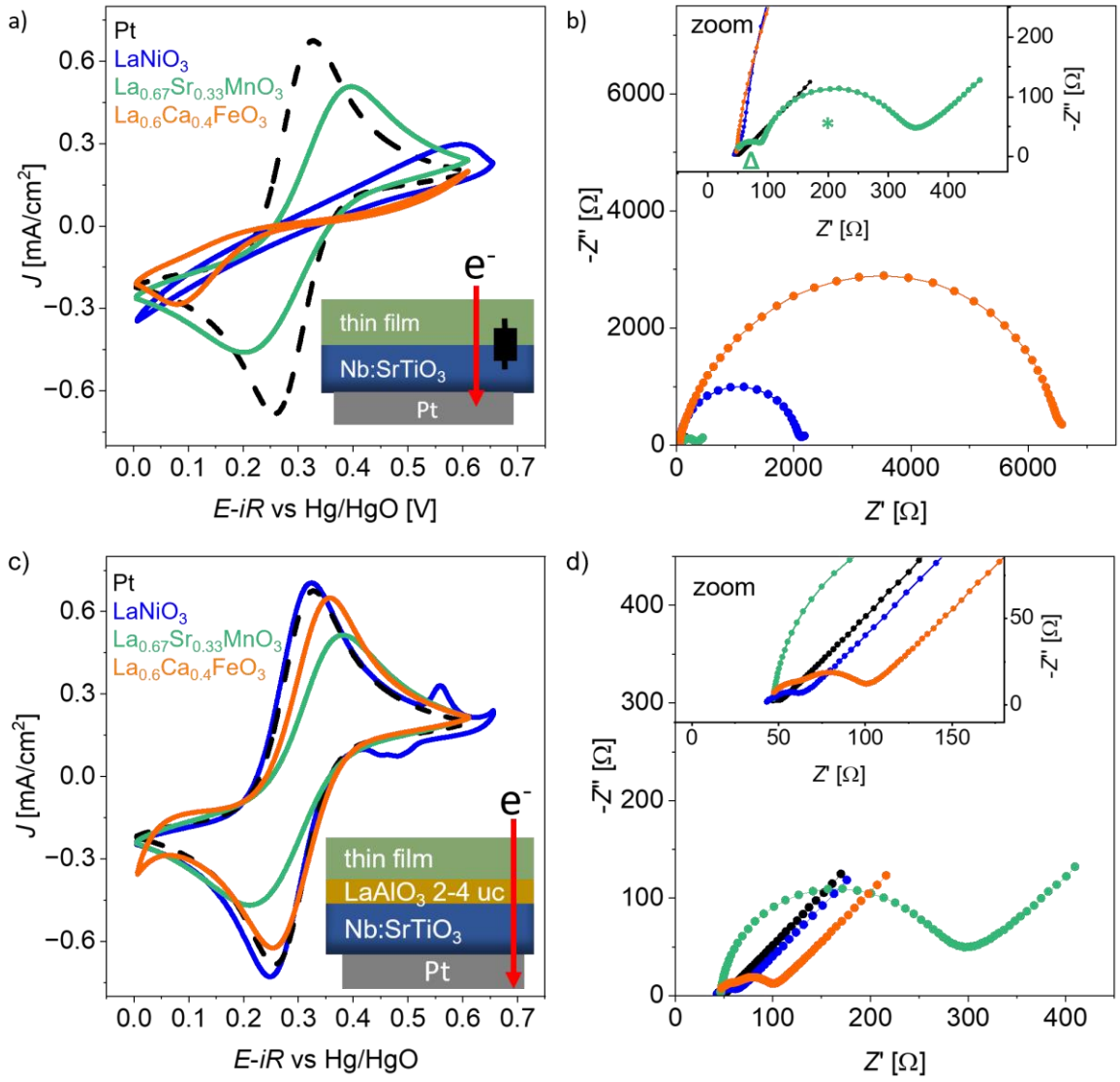

*Figure 3: a) Cyclic voltammetry in Fe^{2+}/Fe^{3+} electrolyte for $LaNiO_{3-\delta}$, $La_{0.67}Sr_{0.33}MnO_{3-\delta}$ and $La_{0.6}Ca_{0.4}FeO_{3-\delta}$ thin films grown on $Nb:SrTiO_3$ in comparison to the platinum sample. b) Corresponding impedance spectra at OCV. Legend corresponds to a). Inset shows the zoom of the lower impedance values. Δ refers to the semi-circle in the high frequency range of $La_{0.67}Sr_{0.33}MnO_{3-\delta}$ and * refers to the semi-circle towards lower frequencies. c) Cyclic voltammetry in Fe^{2+}/Fe^{3+} electrolyte for $Nb:SrTiO_3$/2 uc $LaAlO_3$/ $LaNiO_{3-\delta}$, $Nb:SrTiO_3$/2 uc $LaAlO_3$/ $La_{0.67}Sr_{0.33}MnO_{3-\delta}$ and $Nb:SrTiO_3$/4 uc $LaAlO_3$/ $La_{0.6}Ca_{0.4}FeO_{3-\delta}$ thin films in comparison to the platinum sample. For $LaNiO_{3-\delta}$ additional oxidation and reduction peaks are seen at 0.55 V and 0.45 vs Hg/HgO, respectively, representing the Ni^{2+}/Ni^{3+} redox reaction. d) Corresponding impedance spectra at OCV. Inset shows the zoom to the lower impedance values.*

To suppress electron transport limitations and the large radial current density distribution of the resistive thin film electrocatalysts, the chosen OER catalyst layers were deposited on 0.5 wt% Nb-doped $SrTiO_3$ ($Nb:SrTiO_3$), which possesses metallic conductivity in the bulk. As sketched in **Figure 3a**, the electrons can now travel from the solid/liquid interface directly through the only nanometers thick films into the

Nb:$SrTiO_3$ substrate, which can act as current collector. The film thickness is 10 nm for $LaNiO_{3-\delta}$, 20 nm for $La_{0.6}Ca_{0.4}FeO_{3-\delta}$ and 25 nm for $La_{0.67}Sr_{0.33}MnO_{3-\delta}$ which is far above the thickness where finite size phenomena occur. Here, Pt is only sputtered on the back side of the substrate. In this contacting geometry, $La_{0.6}Ca_{0.4}FeO_{3-\delta}$ and notably also $LaNiO_{3-\delta}$ show largely suppressed current densities and large peak separations in the Fe^{2+}/ Fe^{3+} redox reaction (**Figure 3a**) while the current density of $La_{0.67}Sr_{0.33}MnO_{3-\delta}$ is the closest to the Pt reference and the peak separation is much smaller. This indicates that although the travelling distance has changed from a few millimeters in lateral dimensions to a few nanometers in vertical dimension in this sample geometry, the charge transport remains limited. This is particularly observed for the OER catalyst with lowest ($La_{0.6}Ca_{0.4}FeO_{3-\delta}$) and largest ($LaNiO_{3-\delta}$) conductivity, indicating a departure from the systematic scaling with electrical conductivity as observed before. Instead, the observed behavior suggests an interfacial contact resistance across the substrate/thin film interface,[42–45] resulting from Schottky-type space charge layers.

For a Schottky barrier (the catalyst work function is higher than the Nb:$SrTiO_3$ electron affinity), it is expected that the electron transport is more hampered for the oxidation reaction rather than for the reduction reaction[24]. For $La_{0.6}Ca_{0.4}FeO_{3-\delta}$, the oxidation and reduction peak of Fe^{2+}/ Fe^{3+} are asymmetric, indicating that the (Schottky barrier-type) contact resistance at the Nb:$SrTiO_3$/thin film interface especially hampers the oxidation from Fe^{2+} to Fe^{3+}. Similarly, this is also expected for $LaNiO_{3-\delta}$ as the work function is larger than the Nb:$SrTiO_3$ electron affinity[27]. However, the Ni oxidation takes place in the same measured potential window[32] as the Fe oxidation, therefore the Ni^{3+} and Fe^{3+} formation might lead to additional asymmetric behavior in the anodic sweep compared to the cathodic sweep seen in **Figure 3a**.

The Nyquist plots in **Figure 3b** show large semi-circles for $La_{0.6}Ca_{0.4}FeO_{3-\delta}$ and $LaNiO_{3-\delta}$ with a real impedance (*Z'*) of up to several kΩ which may be attributed to the substrate/thin film contact resistance. In contrast, $La_{0.67}Sr_{0.33}MnO_{3-\delta}$ exhibits two semi-circles that are below 400 Ω (marked with a green * and Δ in the inset of **Figure 3b**), indicating a significantly lower contact resistance at the substrate/thin film interface, consistent with the smaller peak separation and higher current densities in the Fe^{2+}/ Fe^{3+} redox reaction compared to $La_{0.6}Ca_{0.4}FeO_{3-\delta}$ and $LaNiO_{3-\delta}$. The semi-circle in the high frequency range (marked

with Δ) of $La_{0.67}Sr_{0.33}MnO_{3-\delta}$ could stem from the Nb:$SrTiO_3$/thin film interface impedance and the semi-circle towards lower frequencies (*) could stem from $La_{0.67}Sr_{0.33}MnO_{3-\delta}$ -specific and contact-independent behavior as the same order of magnitude impedance was already observed on the insulating substrate (**Figure 2b**).

The Nyquist plots in **Figure 3b** show that R_u is now in the same range of 40-50 Ω for all three materials, indicating that the additional ohmic resistance of the resistive $La_{0.6}Ca_{0.4}FeO_{3-\delta}$ thin film that was observed in **Figure 2b**, is circumvented in this geometry. Nevertheless, the large contact resistance to the substrate, especially for $La_{0.6}Ca_{0.4}FeO_{3-\delta}$ and $LaNiO_{3-\delta}$ still affects the electrochemical performance and thus hinders the observation of intrinsic catalytic properties of the OER.

To decrease the contact resistance between the thin film and Nb:$SrTiO_3$, a 2-4 uc thick interlayer of $LaAlO_3$ was introduced (see sketch in **Figure 3c**; corresponding RHEED data are shown in Figure S6). This polar oxide layer induces an electrical dipole which can counteract interfacial space charge layers and Schottky barriers, facilitating the electron transport across the interface[21,27,46]. We note that the ideal dipole layer thickness to compensate the built-in potentials is specific to the materials at the interface. For the $LaNiO_{3-\delta}$ /Nb:$SrTiO_3$ interface, 2 unit cells (uc) of $LaAlO_3$ as interlayer effectively decreased the contact resistance, as evident by the resulting CV scan in the Fe^{2+}/Fe^{3+} redox couple (**Figure 3c**) and the impedance at OCV (**Figure 3d**), both of which are now similar to the Pt reference (**Figure 3c** and **3d**). This shows a clear improvement in comparison to the $LaNiO_{3-\delta}$/Nb:$SrTiO_3$ sample without $LaAlO_3$ interlayer (**Figure 3a** and **3b**).

In the case of $La_{0.67}Sr_{0.33}MnO_{3-\delta}$, introducing 2 uc of $LaAlO_3$ results in a slightly smaller peak separation as can be seen in the Fe^{2+}/Fe^{3+} CV scan (comparing **Figure 3a** and **3c** with 0.2 V and 0.17 V peak separation, respectively) but still exhibits a small remaining overpotential. Comparing the impedance data of $La_{0.67}Sr_{0.33}MnO_{3-\delta}$ with and without $LaAlO_3$ interlayer on Nb:$SrTiO_3$ in **Figure 3b** and **3d** shows that with the $LaAlO_3$ interlayer, the semi-circle in the high frequency range (Δ) is not visible anymore but the semi-circle marked with a * in **Figure 3b** remains. The $LaAlO_3$ interlayer might have compensated the smaller interface

resistance at the Nb:$SrTiO_3$/$La_{0.67}Sr_{0.33}MnO_{3-\delta}$ interface, but an additional $La_{0.67}Sr_{0.33}MnO_{3-\delta}$-specific impedance behavior remains, which was observed in all contacting geometries.

For $La_{0.6}Ca_{0.4}FeO_{3-\delta}$, a $LaAlO_3$ interlayer thickness of 4 uc was required to sufficiently decrease the Nb:$SrTiO_3$/$La_{0.6}Ca_{0.4}FeO_{3-\delta}$ contact resistance. For the Nb:$SrTiO_3$/$LaAlO_3$/$La_{0.6}Ca_{0.4}FeO_{3-\delta}$ stack, the reduction peak from Fe^{3+} to Fe^{2+} shows now similar behavior as the Pt sample (**Figure 3c**) and the oxidation peak exhibits only a small overpotential. The total impedance was reduced by two orders of magnitude by the 4 uc thick $LaAlO_3$ interlayer comparing the impedance in **Figure 3b** and **3d**. Only two small semi-circles remain that are observed in the Nyquist plot in **Figure 3d**. The small remaining overpotential of the oxidation reaction might stem from a small remaining contact resistance at the Nb:$SrTiO_3$/$LaAlO_3$/ $La_{0.6}Ca_{0.4}FeO_{3-\delta}$ interface and/or from an $La_{0.6}Ca_{0.4}FeO_{3-\delta}$ -specific resistance. As a result, the electrochemical performance in this geometry should not be strongly limited by electronic transport anymore despite the high resistivity of $La_{0.6}Ca_{0.4}FeO_{3-\delta}$. This is evidenced by the high currents obtained with the outer-sphere fast redox couple. Similarly, electronic transport limitations are negligible for electrocatalytic inner-sphere redox reactions such as OER, implying that the measured electrocatalytic current in this geometry directly scales with the intrinsic ability of $La_{0.6}Ca_{0.4}FeO_{3-\delta}$ to catalyze the reaction of interest, here the OER[24].

Hence, the three perovskites grown on Nb:$SrTiO_3$ with $LaAlO_3$ as charge compensating interlayer were tested in 0.1 M KOH to reveal the intrinsic catalytic activity in the OER with minimized electron transport limitations through the bulk and substrate interface resistance. Note that in contrast to the experiments in Fe^{2+}/Fe^{3+} containing electrolyte, RDE rotation is set to 1600 rpm for OER experiments, to remove evolving oxygen gas from the surface during the CV scan. **Figure 4a** shows the corresponding impedance in 0.1 M KOH of the Nb:$SrTiO_3$/$LaAlO_3$/catalyst stacks. The R_u is small (40-50 Ω) for the three perovskite oxides indicating no significant ohmic losses through bulk resistivities are present, which is consistent with the observation of the impedance in the Fe^{2+}/ Fe^{3+} containing electrolyte. For $La_{0.6}Ca_{0.4}FeO_{3-\delta}$, there is a small semi-circle observed (~20 Ω) in the high frequency range which can stem from a small remaining contact resistance at the $La_{0.6}Ca_{0.4}FeO_{3-\delta}$/$LaAlO_3$/Nb:$SrTiO_3$ interface. Overall, however, the R_u and the

contact resistances to the substrate show significantly lower absolute values than observed in the initial in-plane geometry and $LaAlO_3$ free thin film stacks on $Nb:SrTiO_3$, indicating a successful removal of the OER-performance limiting current paths.

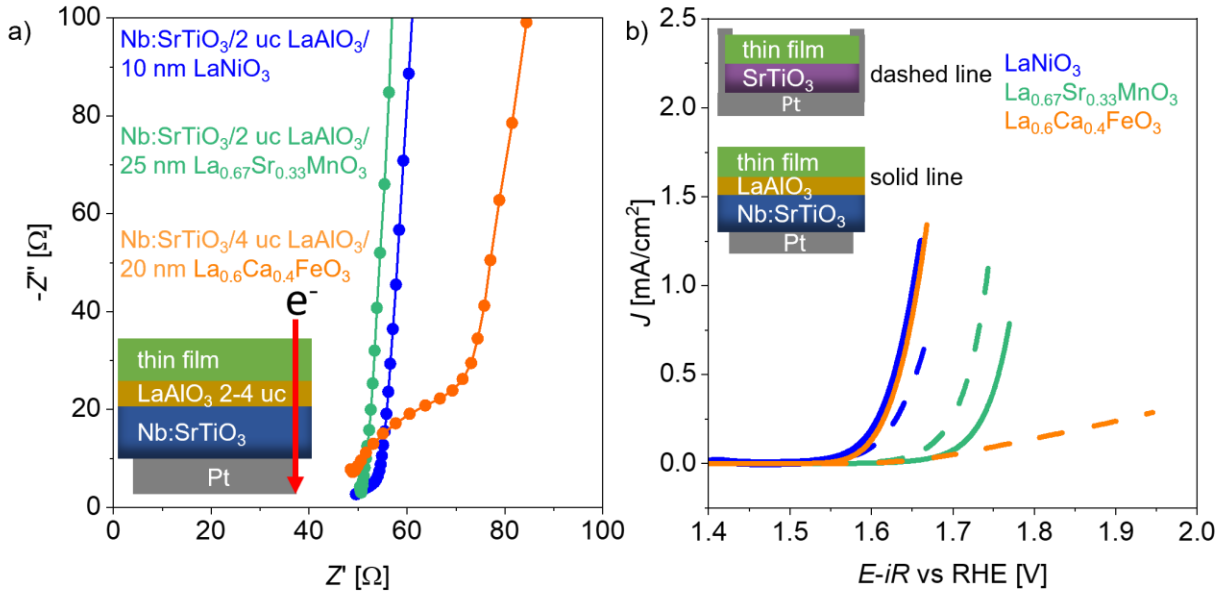

Figure 4: a) Impedance spectra in the high frequency range at OCV for the thin films on $Nb:SrTiO_3$ with $LaAlO_3$ interlayer recorded in 0.1 M KOH solution. b) OER catalytic activity of $LaNiO_{3-\delta}$, $La_{0.67}Sr_{0.33}MnO_{3-\delta}$ and $La_{0.6}Ca_{0.4}FeO_{3-\delta}$ thin films in 0.1 M KOH for the two different contacting geometries sketched in the top left corner. OER performance on the insulating STO substrates are shown as dashed lines (reproduced from Figure 1c for ease of comparison) and OER activities of $Nb:SrTiO_3$/2 uc $LaAlO_3/LaNiO_{3-\delta}$, $Nb:SrTiO_3$/2 uc $LaAlO_3/La_{0.67}Sr_{0.33}MnO_{3-\delta}$ and $Nb:SrTiO_3$/4 uc $LaAlO_3/La_{0.6}Ca_{0.4}FeO_{3-\delta}$ stacks are shown as solid lines.

Figure 4b shows the OER activity comparison of the two different contacting geometries, $SrTiO_3$/catalyst and $Nb:SrTiO_3/LaAlO_3$/catalyst. The $SrTiO_3/LaNiO_{3-\delta}$ and $Nb:SrTiO_3/LaAlO_3/LaNiO_{3-\delta}$ stacks show a similar η of 0.37 V and 0.36 V at 0.1 mA/cm^2, respectively. $La_{0.67}Sr_{0.33}MnO_{3-\delta}$ shows a higher η than $LaNiO_{3-\delta}$ in both contacting geometries with η = 0.44 V and 0.48 V at 0.1 mA/cm^2 for the $SrTiO_3/La_{0.67}Sr_{0.33}MnO_{3-\delta}$ and $Nb:SrTiO_3/LaAlO_3/La_{0.67}Sr_{0.33}MnO_{3-\delta}$ stacks, respectively. The deviation between the samples can occur because of small remaining contact resistances to the $Nb:SrTiO_3$ substrate or because of sample-to-sample deviation. $La_{0.6}Ca_{0.4}FeO_{3-\delta}$ exhibits very high η on the insulating substrate (0.53 V at 0.1 mA/cm^2, as already introduced in **Figure 1b**), but the $Nb:SrTiO_3/LaAlO_3/ La_{0.6}Ca_{0.4}FeO_{3-\delta}$ stack shows remarkably low η of 0.36 V at 0.1 mA/cm^2, which is similar to $LaNiO_{3-\delta}$. Hence, $La_{0.6}Ca_{0.4}FeO_{3-\delta}$ exhibits a similar intrinsic catalytic

activity in the OER as $LaNiO_{3-\delta}$, although it has three orders of magnitude higher resistivity. In turn, $La_{0.67}Sr_{0.33}MnO_{3-\delta}$ - exhibiting intermediate resistivity among the three tested perovskites - shows the lowest intrinsic OER catalytic activity compared to $LaNiO_{3-\delta}$ and $La_{0.6}Ca_{0.4}FeO_{3-\delta}$. As a result, the intrinsic OER activity of the perovskite oxides does not scale monotonically with their electronic resistivity, and in fact, even a high resistivity perovskite can exhibit high OER performance – a result that could not have been revealed without dedicated and systematic choice of the sample substrate and interfacial layers.

Discussion

By tuning the bulk electron transport from millimeter to nanometer scales, and additionally minimizing the contact resistance in the sample stack, the intrinsic catalytic properties in the OER could be revealed for $LaNiO_{3-\delta}$, $La_{0.67}Sr_{0.33}MnO_{3-\delta}$ and even for the highly resistive $La_{0.6}Ca_{0.4}FeO_{3-\delta}$. The observed OER overpotential trend changes from $\eta(LaNiO_{3-\delta}) < \eta(La_{0.67}Sr_{0.33}MnO_{3-\delta}) < \eta(La_{0.6}Ca_{0.4}FeO_{3-\delta})$, as observed in resistance-dominated geometry with inhomogeneous current contribution across the catalyst interface, to $\eta(LaNiO_{3-\delta}) \approx \eta(La_{0.6}Ca_{0.4}FeO_{3-\delta}) < \eta(La_{0.67}Sr_{0.33}MnO_{3-\delta})$ as intrinsic catalytic activity trend. Hence, the intrinsic properties of perovskite catalysts do not necessarily scale with their resistivity when the catalyst bulk electron transport is limited to small distances.

However, even small residual interface resistances like the remaining interface resistance of around 20 Ω at the $Nb:SrTiO_3/LaAlO_3/ La_{0.6}Ca_{0.4}FeO_{3-\delta}$ interface might affect the overall observed overpotential, diluting the revelation of intrinsic properties. This is especially noticeable at higher current densities. For small currents such as 0.1 mA, a 20 Ω series resistance leads to 2 mV additional ohmic overpotential, whereas for 10 mA this already leads to 200 mV ohmic overpotential. Additionally, as such Schottky-barrier-type resistances are voltage dependent, the interface resistance might change with applied potential, which might dilute the revelation of intrinsic properties as well.

A similar OER activity trend compared to our findings for the $Nb:SrTiO_3/LaAlO_3$/thin film stacks was obtained for $LaNiO_{3-\delta}$, $La_{0.75}Ca_{0.25}FeO_{3-\delta}$, $La_{0.5}Ca_{0.5}FeO_{3-\delta}$ and $La_{0.5}Ca_{0.5}MnO_{3-\delta}$ at 50 $\mu A/cm^2$ by Suntivich *et al.* in powder experiments (grain size 0.2-1.0 µm) with conductive carbon[5]. In their study, a

lower activity was observed also for the manganite $La_{0.5}Ca_{0.5}MnO_{3-\delta}$ compared to the nickelate and calcium doped ferrates (η ($LaNiO_{3-\delta}$) ≈ η ($La_{0.5}Ca_{0.5}FeO_{3-\delta}$) < η ($La_{0.5}Ca_{0.5}MnO_{3-\delta}$)). In contrast, it is also reported in the literature that especially $La_{0.6}Ca_{0.4}FeO_{3-\delta}$ in the solid solution series of $La_{1-x}Ca_xFeO_{3-\delta}$ has a low catalytic activity[47] with an overpotential (at 50 µA/cm^2) comparable to what we observed for $La_{0.6}Ca_{0.4}FeO_{3-\delta}$ on the insulating substrate with a long bulk electron transport pathway. One reason for the higher overpotentials observed (compared to our Nb:$SrTiO_3$/$LaAlO_3$/$La_{0.6}Ca_{0.4}FeO_{3-\delta}$ sample and to the findings of Suntivich *et al*.) could be a larger grain size in the catalyst powder of the highly resistive $La_{0.6}Ca_{0.4}FeO_{3-\delta}$. This could extend the electron transport pathway through the powder bulk significantly even with conductive carbon, so that larger current losses occur. Additionally, conductive carbon can, for example, change the valence state of the B-site or can act as a co-catalyst[8,48,49], hindering to reveal intrinsic catalytic properties as well.

Our findings and the comparison to the literature indicate that the establishment of catalyst design rules must be taken with care, especially when materials across large resistivity ranges are tested and substrate-to-catalyst contact resistances occur. One design rule addressed in the literature stems from the observation that a small charge transfer energy leads to higher OER activity[11]. However, a large charge transfer energy (which is the energy distance between the occupied O 2p and first unoccupied transition metal 3d states) typically also leads to a lower conductivity, which can lead to lower measured (but not lower intrinsic) OER activity[11]. Therefore, it is crucial not to assume a direct correlation between low conductivity and low OER catalytic activity, which has become obvious from our revelation that metal oxides with low conductivity can exhibit high catalytic activity. Extra steps have to be taken to disentangle intrinsic catalytic activity from conductivity to accurately assess performance. As we have shown, this can be achieved using epitaxial model systems with appropriate current collectors and favorable interface properties.

Conclusion

We have shown that highly resistive perovskite oxides can be intrinsically as active as quasi metallic electrocatalysts in the OER. We decoupled the bulk resistivity and substrate/thin film contact resistances from intrinsic catalytic processes at the solid/liquid interface for the three perovskites $LaNiO_{3-\delta}$, $La_{0.67}Sr_{0.33}MnO_{3-\delta}$ and $La_{0.6}Ca_{0.4}FeO_{3-\delta}$ by keeping the electron transport pathway through the catalyst bulk on the nanometer scale and minimizing the contact resistance to the $Nb:SrTiO_3$ substrate. Through insertion of a $LaAlO_3$ dipole layer, the contact resistance between $NbSrTiO_3$ and catalyst was strongly decreased. Thus, we could reveal that $LaNiO_{3-\delta}$ and $La_{0.6}Ca_{0.4}FeO_{3-\delta}$ have similar intrinsic catalytic properties, even though $La_{0.6}Ca_{0.4}FeO_{3-\delta}$ has 3 orders of magnitude higher resistivity compared to $LaNiO_{3-\delta}$. $La_{0.67}Sr_{0.33}MnO_{3-\delta}$ has intrinsically a lower OER activity compared to $La_{0.6}Ca_{0.4}FeO_{3-\delta}$ and $LaNiO_{3-\delta}$. Hence, electrical conductivity does not necessarily correlate with intrinsic catalytic properties. Therefore, it is of high importance to quantify electron pathway dependent current density losses in chosen sample geometries as well as to distinguish intrinsic properties from resistivity for the establishment of OER catalyst design rules.

Experimental Methods:

Thin film fabrication: The epitaxial thin films were deposited by PLD on single crystal $SrTiO_3$ and Nb:$SrTiO_3$ 10x10 mm^2 substrates in (100) orientation. $LaNiO_{3-\delta}$ was grown with a fluence of 1.9 J/cm^2 with a pulse repetition rate of 2 Hz, with a target to substrate distance of 50 mm and with an oxygen partial pressure of 0.04 mbar at 450 °C (650°C respectively for the sample discussed in Figs. 2a,b. The growth temperature can have an influence on the catalytic activity but does not drastically change the conductivity that is important for the Fe^{2+}/Fe^{3+} CV experiment[32]). $La_{0.67}Sr_{0.33}MnO_{3-\delta}$ was grown with a fluence of 2 J/cm^2, with a pulse repetition rate of 2 Hz and target to substrate distance of 50 mm at a growth temperature of 750 °C and oxygen partial pressure of 0.266 mbar. The $LaAlO_3$ interlayer between Nb:$SrTiO_3$ and $LaNiO_{3-\delta}$ and $La_{0.67}Sr_{0.33}MnO_{3-\delta}$ respectively was grown with a fluence of 1.4 J/cm^2, 1 Hz pulse repetition rate at a growth temperature of 650 °C and an oxygen partial pressure of 0.002 mbar. $La_{0.6}Ca_{0.4}FeO_{3-\delta}$ was deposited at 650 °C, with a laser fluence of 2.2 J/cm^2 and oxygen partial pressure of 0.05 mbar, and the target to substrate distance was 55 mm. An $LaAlO_3$ interlayer was grown on Nb:$SrTiO_3$ at 700 °C with 1.8 J/cm^2 laser fluence and $1x10^{-4}$ mbar oxygen partial pressure.

Physical characterization: Atomic force microscopy scans were recorded with a Cypher SPM (Research Asylum, Germany) atomic force microscope in tapping mode. XRD was conducted with a D8 ADVANCE diffractometer (Bruker AXS GmbH, Germany) that is equipped with a Cu cathode for K_α radiation and the scans were recorded in 2θ-ω geometry.

Electrochemical characterization: To ensure electrical contact in the electrochemical cell, the samples deposited on $SrTiO_3$ were sputtered with 50 nm Pt on the backside, edges and front edges (as shown in the SI Figure S2). Samples grown on Nb:$SrTiO_3$ were sputtered only from the back side. Electrochemical measurements of the thin films were conducted with a RDE with a rotation speed of 1600 rpm in a three-electrode configuration in 0.1 M KOH. The KOH pellets were provided from Sigma Aldrich (purity 99.99 %) and dissolved in deionized water (Milli-Q, >18.2 MΩcm). The counter electrode was a spiraled Pt wire. The reference electrode was a Hg/HgO electrode protected from the solution by a Teflon tube filled with 1 M KOH. The thin films were mounted on the RDE with a custom-made PEEK holder. The thin film back side and front edges were sealed with an O-ring from the electrolyte. Here, the back of the substrate is mechanically pressed against the rotary shaft of the RDE. The geometric surface area that is exposed to the electrolyte is equal to the inner area of the O-ring.

Before determining the OER activity with CV, impedance spectroscopy was recorded at OCV and double layer capacitance measurements were conducted in the range from 0.0 to 0.1 V vs Hg/HgO (for $La_{0.6}Ca_{0.4}FeO_{3-\delta}$ from 0.1 to 0.2 V) with an increasing scan rate from 10 to 500 mV/s. To record the redox behavior of $LaNiO_{3-\delta}$ thin films, the potential window from 0.2 to 0.65 V vs Hg/HgO was recorded with an increasing scan rate from 10 to 500 mV/s. To determine the OER activity, CV scans were conducted from

0.2 V up to 1.15 V vs Hg/HgO to reach at least 0.5 mA/cm^2. The Hg/HgO electrode was calibrated against the RHE (HydroFlex, USA). The averaged value of 0.887 V vs Hg/HgO was used to determine the obtained voltage on the RHE scale. The impedance was recorded in a frequency range of 100 kHz to 0.1 Hz with an amplitude of 20 mV. As the uncompensated resistance is observed in the range of 10 kHz, the spectra are shown for data points from 10 kHz and below (see for clarity SI Figure S3). Electrochemical measurements with the Fe^{2+}/Fe^{3+} redox couple were conducted in a 0.1 M KOH solution with an equimolar concentration of of 0.003 mol/l of $K_4[Fe(CN)_6]$ [H_2O] and $K_3[Fe(CN)_6]$ (Sigma Aldrich (99.5 % and 99.0%). The RDE rotation was off for the experiments in the Fe^{2+}/Fe^{3+} containing electrolyte. Impedance was recorded at OCV and CV scans were recorded between 0-0.6 V vs Hg/HgO. For $LaNiO_{3-\delta}$ the window was extended to 0.65 V to obtain a possible contribution from Ni oxidation.

COMSOL study: Simulations for the current density distribution along the film/electrolyte interface were carried out in COMSOL Multiphysics® 6.2 by using the Electric Currents (ec) module. A detailed sketch, description of the simulation and the corresponding parameter values can be found in the SI Figure S4. Current is injected from the Pt back electrode of the substrate and travels to the thin film edge and subsequently to the sample center with resistivities as listed in the main text. The electrons travel through an interfacial boundary layer to the electrolyte with a resistance that was set to 100 Ω, representing typical charge transfer resistances at low applied voltage. Finally, they travel through the electrolyte to the counter electrode (ground). As the thin film has a large aspect ratio (25 nm thickness vs 3.75 cm length, i.e. the distance from the sample center to the O-ring), initial coarse simulations were carried out to optimize the geometry and mesh as much as possible. Here, we used a 2D axisymmetric geometry to further reduce the amount of mesh elements. As expected, since the substrate has a very large resistance, no current flows from the Pt electrode through the substrate itself. Hence, in the final model, the substrate was removed to reduce the amount of mesh elements. A combination of free quad and boundary layer meshes was used to create a mesh with a high quality while keeping the number of meshing elements in a reasonable range (mesh sketch can be found in the SI Figure S4). The current densities $J_z(x)$ shown in Figure 2c are extracted by a line cut at the boundary between the thin film and the electrolyte.

Acknowledgements:

We thank Grigory Potemkin, Shreyas Harsha, and Tursun Abudukade for the experimental support. We gratefully acknowledge funding from the European Union (ERC, 101040669 - Interfaces at Work). Views and opinions expressed are however those of the author(s) only and do not necessarily reflect those of the European Union or the European Research Council. Neither the European Union nor the granting authority can be held responsible for them.

Author contribution:

L.H., I.v.d.B., F.G. and C.B. conceived and designed the experiments. L.H. and I.v.d.B conducted electrochemical experiments. L.H., I.v.d.B., E.v.d.M. and E.K. fabricated the thin film samples. L.H. and E.v.d.M. conducted resistivity measurements. D.W. conceptualized and conducted the COMSOL simulations. D.S. and S.M. refined the mesh of the COMSOL model. O.K. and A.K. provided experimental support and scientific discussion. B.B. advised on an in-depth understanding of impedance data. L.H., I.v.d.B., B.B., F.G. and C.B. conducted in-depth scientific discussions on electrochemical and physical analysis during the whole experimental progress. L.H., I.v.d.B., D.W., F.G. and C.B. wrote the manuscript with contributions from all authors. F.G. and C.B. supervised the research project.

(1) International Energy Agency. *The Future of Hydrogen*; International Energy Agency (IEA), 2019. https: //www.iea.org/reports/the-future-of-hydrogen.

(2) Carrara, S.; Bobba, S.; Blagoeva, D.; Alves Dias, P.; Cavalli, A.; Georgitzikis, K.; Grohol, K.; Itul, A.; Kuzov, T.; Latunussa, C.; Lyons, L.; Malano, G.; Maury, T.; Prior Arce, A.; Somers, J.; Telsnig, T.; Veeh, C.; Wittmer, D.; Black, C.; Pennington, D.; Christou, M. *Supply Chain Analysis and Material Demand Forecast in Strategic Technologies and Sectors in the EU – A Foresight Study*; Policy assessment, Anticipation and foresight, Risk assessment KJ-NA-31-437-EN-N (online),KJ-NA-31-437-EN-C (print); Publications Office of the European Union: Luxembourg (Luxembourg), 2023. https://doi.org/10.2760/386650 (online),10.2760/334074 (print).

(3) Xie, X.; Du, L.; Yan, L.; Park, S.; Qiu, Y.; Sokolowski, J.; Wang, W.; Shao, Y. Oxygen Evolution Reaction in Alkaline Environment: Material Challenges and Solutions. *Advanced Functional Materials* **2022**, *32* (21), 2110036. https://doi.org/10.1002/adfm.202110036.

(4) Liu, J.; Liu, H.; Chen, H.; Du, X.; Zhang, B.; Hong, Z.; Sun, S.; Wang, W. Progress and Challenges Toward the Rational Design of Oxygen Electrocatalysts Based on a Descriptor Approach. *Advanced Science* **2020**, *7* (1), 1901614. https://doi.org/10.1002/advs.201901614.

(5) Suntivich, J.; May, K. J.; Gasteiger, H. A.; Goodenough, J. B.; Shao-Horn, Y. A Perovskite Oxide Optimized for Oxygen Evolution Catalysis from Molecular Orbital Principles. *Science* **2011**, *334* (6061), 1383–1385. https://doi.org/10.1126/science.1212858.

(6) Gunkel, F.; Christensen, D. V.; Chen, Y. Z.; Pryds, N. Oxygen Vacancies: The (in)Visible Friend of Oxide Electronics. *Applied Physics Letters* **2020**, *116* (12), 120505. https://doi.org/10.1063/1.5143309.

(7) George, G., Ede, S.R., & Luo, Z., C. Press. *Fundamentals of Perovskite Oxides: Synthesis, Structure, Properties and Applications (1st Ed.)*; 2020.

(8) Liu, L.-B.; Yi, C.; Mi, H.-C.; Zhang, S. L.; Fu, X.-Z.; Luo, J.-L.; Liu, S. Perovskite Oxides Toward Oxygen Evolution Reaction: Intellectual Design Strategies, Properties and Perspectives. *Electrochemical Energy Reviews* **2024**, *7* (1), 14. https://doi.org/10.1007/s41918-023-00209-2.

(9) Lakhanlal; Caspary Toroker, M. Filling the Gaps on the Relation between Electronic Conductivity and Catalysis of Electrocatalysts for Water Splitting Using Computational Modelling. *Current Opinion in Electrochemistry* **2023**, *40*, 101342. https://doi.org/10.1016/j.coelec.2023.101342.

(10) Cheng, X.; Fabbri, E.; Yamashita, Y.; Castelli, I. E.; Kim, B.; Uchida, M.; Haumont, R.; Puente-Orench, I.; Schmidt, T. J. Oxygen Evolution Reaction on Perovskites: A Multieffect Descriptor Study Combining Experimental and Theoretical Methods. *ACS Catal.* **2018**, *8* (10), 9567–9578. https://doi.org/10.1021/acscatal.8b02022.

(11) Hong, W. T.; Stoerzinger, K. A.; Lee, Y.-L.; Giordano, L.; Grimaud, A.; Johnson, A. M.; Hwang, J.; Crumlin, E. J.; Yang, W.; Shao-Horn, Y. Charge-Transfer-Energy-Dependent Oxygen Evolution Reaction Mechanisms for Perovskite Oxides. *Energy Environ. Sci.* **2017**, *10* (10), 2190–2200. https://doi.org/10.1039/C7EE02052J.

(12) Egelund, S.; Caspersen, M.; Nikiforov, A.; Møller, P. Manufacturing of a $LaNiO_3$ Composite Electrode for Oxygen Evolution in Commercial Alkaline Water Electrolysis. *International Journal of Hydrogen Energy* **2016**, *41* (24), 10152–10160. https://doi.org/10.1016/j.ijhydene.2016.05.013.

(13) Zou, S.; Burke, M. S.; Kast, M. G.; Fan, J.; Danilovic, N.; Boettcher, S. W. Fe (Oxy)Hydroxide Oxygen Evolution Reaction Electrocatalysis: Intrinsic Activity and the Roles of Electrical Conductivity, Substrate, and Dissolution. *Chem. Mater.* **2015**, *27* (23), 8011–8020. https://doi.org/10.1021/acs.chemmater.5b03404.

(14) Burke, M. S.; Enman, L. J.; Batchellor, A. S.; Zou, S.; Boettcher, S. W. Oxygen Evolution Reaction Electrocatalysis on Transition Metal Oxides and (Oxy)Hydroxides: Activity Trends and Design Principles. *Chem. Mater.* **2015**, *27* (22), 7549–7558. https://doi.org/10.1021/acs.chemmater.5b03148.

(15) Fan, L.; Rautama, E. L.; Lindén, J.; Sainio, J.; Jiang, H.; Sorsa, O.; Han, N.; Flox, C.; Zhao, Y.; Li, Y.; Kallio, T. Two Orders of Magnitude Enhancement in Oxygen Evolution Reactivity of $La_{0.7}Sr_{0.3}Fe_{1-x}Ni_xO_{3-\delta}$ by Improving the Electrical Conductivity. *Nano Energy* **2022**, *93*, 106794. https://doi.org/10.1016/j.nanoen.2021.106794.

(16) Stoerzinger, K. A.; Choi, W. S.; Jeen, H.; Lee, H. N.; Shao-Horn, Y. Role of Strain and Conductivity in Oxygen Electrocatalysis on $LaCoO_3$ Thin Films. *J. Phys. Chem. Lett.* **2015**, *6* (3), 487–492. https://doi.org/10.1021/jz502692a.

(17) Yun, T. G.; Heo, Y.; Bin Bae, H.; Chung, S.-Y. Elucidating Intrinsic Contribution of D-Orbital States to Oxygen Evolution Electrocatalysis in Oxides. *Nature Communications* **2021**, *12* (1), 824. https://doi.org/10.1038/s41467-021-21055-0.

(18) Heymann, L.; Weber, M. L.; Wohlgemuth, M.; Risch, M.; Dittmann, R.; Baeumer, C.; Gunkel, F. Separating the Effects of Band Bending and Covalency in Hybrid Perovskite Oxide Electrocatalyst Bilayers for Water Electrolysis. *ACS Appl. Mater. Interfaces* **2022**, *14* (12), 14129–14136. https://doi.org/10.1021/acsami.1c20337.

(19) Akbashev, A. R.; Zhang, L.; Mefford, J. T.; Park, J.; Butz, B.; Luftman, H.; Chueh, W. C.; Vojvodic, A. Activation of Ultrathin $SrTiO_3$ with Subsurface $SrRuO_3$ for the Oxygen Evolution Reaction. *Energy Environ. Sci.* **2018**, *11* (7), 1762–1769. https://doi.org/10.1039/C8EE00210J.

(20) Baniecki, J. D.; Yamaguchi, H.; Harnagea, C.; Ricinschi, D.; Gu, Z.; Spanier, J. E.; Yamazaki, T.; Aso, H. Enhanced Stability and Thickness-Independent Oxygen Evolution Electrocatalysis of Heterostructured Anodes with Buried Epitaxial Bilayers. *Advanced Energy Materials* **2019**, *9* (28), 1803846. https://doi.org/10.1002/aenm.201803846.

(21) Yajima, T.; Hikita, Y.; Minohara, M.; Bell, C.; Mundy, J. A.; Kourkoutis, L. F.; Muller, D. A.; Kumigashira, H.; Oshima, M.; Hwang, H. Y. Controlling Band Alignments by Artificial Interface Dipoles at Perovskite Heterointerfaces. *Nature Communications* **2015**, *6* (1), 6759. https://doi.org/10.1038/ncomms7759.

(22) Burton, A. R.; Paudel, R.; Matthews, B.; Sassi, M.; Spurgeon, S. R.; Farnum, B. H.; Comes, R. B. Thickness Dependent OER Electrocatalysis of Epitaxial $LaFeO_3$ Thin Films. *J. Mater. Chem. A* **2022**, *10* (4), 1909–1918. https://doi.org/10.1039/D1TA07142D.

(23) Weber, M. L.; Gunkel, F. Epitaxial Catalysts for Oxygen Evolution Reaction: Model Systems and Beyond. *Journal of Physics: Energy* **2019**, *1* (3), 031001. https://doi.org/10.1088/2515-7655/ab1577.

(24) Antipin, D.; Risch, M. Trends of Epitaxial Perovskite Oxide Films Catalyzing the Oxygen Evolution Reaction in Alkaline Media. *Journal of Physics: Energy* **2020**, *2* (3), 032003. https://doi.org/10.1088/2515-7655/ab812f.

(25) Adiga, P.; Stoerzinger, K. A. Epitaxial Oxide Thin Films for Oxygen Electrocatalysis: A Tutorial Review. *Journal of Vacuum Science & Technology A* **2022**, *40* (1), 010801. https://doi.org/10.1116/6.0001429.

(26) Füngerlings, A.; Wohlgemuth, M.; Antipin, D.; van der Minne, E.; Kiens, E. M.; Villalobos, J.; Risch, M.; Gunkel, F.; Pentcheva, R.; Baeumer, C. Crystal-Facet-Dependent Surface Transformation Dictates the Oxygen Evolution Reaction Activity in Lanthanum Nickelate. *Nature Communications* **2023**, *14* (1), 8284. https://doi.org/10.1038/s41467-023-43901-z.

(27) Nishio, K.; Shirasawa, T.; Shimizu, K.; Nakamura, N.; Watanabe, S.; Shimizu, R.; Hitosugi, T. Tuning the Schottky Barrier Height at the Interfaces of Metals and Mixed Conductors. *ACS Appl. Mater. Interfaces* **2021**, *13* (13), 15746–15754. https://doi.org/10.1021/acsami.0c18656.

(28) Sergeenkov, S.; Cichetto, L.; Zampieri, M.; Longo, E.; Araújo-Moreira, F. M. Scaling like Behaviour of Resistivity Observed in $LaNiO_3$ Thin Films Grown on $SrTiO_3$ Substrate by Pulsed Laser Deposition. *Journal of Physics: Condensed Matter* **2015**, *27* (48), 485307. https://doi.org/10.1088/0953-8984/27/48/485307.

(29) Yin, H. Q.; Zhou, J.-S.; Goodenough, J. B. Near-Room-Temperature Tunneling Magnetoresistance in a Trilayer $La_{0.67}Sr_{0.33}MnO_3/La_{0.85}Sr_{0.15}MnO_3/La_{0.67}Sr_{0.33}MnO_3$ Device. *Applied Physics Letters* **2000**, *77* (5), 714–716. https://doi.org/10.1063/1.127095.

(30) Boschker, H.; Huijben, M.; Vailionis, A.; Verbeeck, J.; Aert, S. van; Luysberg, M.; Bals, S.; Tendeloo, G. van; Houwman, E. P.; Koster, G.; Blank, D. H. A.; Rijnders, G. Optimized Fabrication of High-Quality $La_{0.67}Sr_{0.33}MnO_3$ Thin Films Considering All Essential Characteristics. *Journal of Physics D: Applied Physics* **2011**, *44* (20), 205001. https://doi.org/10.1088/0022-3727/44/20/205001.

(31) Irmak, A. E. Structural and Electrical Properties of Ca^{2+} Doped $LaFeO_3$: The Effect of A-Site Cation Size Mismatch. *Engineering, Technology & Applied Science Research* **2020**, *Vol. 10* (No. 2), 5538–5546.

(32) Baeumer, C.; Li, J.; Lu, Q.; Liang, A. Y.-L.; Jin, L.; Martins, H. P.; Duchoň, T.; Glöß, M.; Gericke, S. M.; Wohlgemuth, M. A.; Giesen, M.; Penn, E. E.; Dittmann, R.; Gunkel, F.; Waser, R.; Bajdich, M.; Nemšák, S.; Mefford, J. T.; Chueh, W. C. Tuning Electrochemically Driven Surface Transformation in Atomically Flat $LaNiO_3$ Thin Films for Enhanced Water Electrolysis. *Nature Materials* **2021**, *20* (5), 674–682. https://doi.org/10.1038/s41563-020-00877-1.

(33) Tran, A.-T.; Huet, F.; Ngo, K.; Rousseau, P. Artefacts in Electrochemical Impedance Measurement in Electrolytic Solutions Due to the Reference Electrode. *Electrochimica Acta* **2011**, *56* (23), 8034–8039. https://doi.org/10.1016/j.electacta.2010.12.088.

(34) Davies, T. J.; Banks, C. E.; Compton, R. G. Voltammetry at Spatially Heterogeneous Electrodes. *Journal of Solid State Electrochemistry* **2005**, *9* (12), 797–808. https://doi.org/10.1007/s10008-005-0699-x.

(35) Muralidharan, V. B. Warburg Impedance - Basics Revisited. *Anti-Corrosion Methods and Materials* **1997**, *44* (1), 26–29.

(36) Hirschorn, B.; Orazem, M. E.; Tribollet, B.; Vivier, V.; Frateur, I.; Musiani, M. Determination of Effective Capacitance and Film Thickness from Constant-Phase-Element Parameters. *Electrochimica Acta* **2010**, *55* (21), 6218–6227. https://doi.org/10.1016/j.electacta.2009.10.065.

(37) Huang, V. M.-W.; Vivier, V.; Orazem, M. E.; Pébère, N.; Tribollet, B. The Apparent Constant-Phase-Element Behavior of a Disk Electrode with Faradaic Reactions: A Global and Local Impedance

Analysis. *Journal of The Electrochemical Society* **2006**, *154* (2), C99. https://doi.org/10.1149/1.2398894.

(38) Pospisil, J.; Marackova, L.; Zmeskal, O.; Kovalenko, A. Universal Approach for Diffusion Quantification Applied to Lead Halide Perovskite Single Crystals. *Applied Physics A* **2023**, *129* (2), 129. https://doi.org/10.1007/s00339-023-06398-3.

(39) Oldham, K. B. Edge Effects in Semiinfinite Diffusion. *Journal of Electroanalytical Chemistry and Interfacial Electrochemistry* **1981**, *122*, 1–17. https://doi.org/10.1016/S0022-0728(81)80136-2.

(40) Balaya, P.; Jamnik, J.; Fleig, J.; Maier, J. Mesoscopic Hole Conduction in Nanocrystalline SrTiO3 : A Detailed Analysis by Impedance Spectroscopy. *Journal of The Electrochemical Society* **2007**, *154* (6), P69. https://doi.org/10.1149/1.2716555.

(41) Menke, T.; Meuffels, P.; Dittmann, R.; Szot, K.; Waser, R. Separation of Bulk and Interface Contributions to Electroforming and Resistive Switching Behavior of Epitaxial Fe-Doped SrTiO3. *Journal of Applied Physics* **2009**, *105* (6), 066104. https://doi.org/10.1063/1.3100209.

(42) Chien, T.; Liu, J.; Yost, A. J.; Chakhalian, J.; Freeland, J. W.; Guisinger, N. P. Built-in Electric Field Induced Mechanical Property Change at the Lanthanum Nickelate/Nb-Doped Strontium Titanate Interfaces. *Scientific Reports* **2016**, *6* (1), 19017. https://doi.org/10.1038/srep19017.

(43) Yoo, H. K.; Chang, Y. J.; Moreschini, L.; Kim, H.-D.; Sohn, C. H.; Sinn, S.; Oh, J. S.; Kuo, C.-T.; Bostwick, A.; Rotenberg, E.; Noh, T. W. Insulating-Layer Formation of Metallic $LaNiO_3$ on Nb-Doped $SrTiO_3$ Substrate. *Applied Physics Letters* **2015**, *106* (12), 121601. https://doi.org/10.1063/1.4916225.

(44) Lu, H. X.; Zhang, J.; Zhang, H. R.; Li, Y.; Chen, Y. S.; Shen, B. G.; Sun, J. R. A Conductive Scanning Study of $La_{0.67}Sr_{0.33}MnO_3$/Nb:$SrTiO_3$ Hetero-Junction. *Applied Physics Letters* **2016**, *108* (5), 051608. https://doi.org/10.1063/1.4941419.

(45) Zhan, J. M.; Li, P. G.; Liu, H.; Tao, S. L.; Ma, H.; Shen, J. Q.; Pan, M. J.; Zhang, Z. J.; Wang, S. L.; Yuan, G. L. Carrier Tuning the Metal-Insulator Transition of Epitaxial $La_{0.67}Sr_{0.33}MnO_3$ Thin Film on Nb Doped $SrTiO_3$ Substrate. *AIP Advances* **2016**, *6* (4), 045001. https://doi.org/10.1063/1.4945694.

(46) Hikita, Y.; Nishio, K.; Seitz, L. C.; Chakthranont, P.; Tachikawa, T.; Jaramillo, T. F.; Hwang, H. Y. Band Edge Engineering of Oxide Photoanodes for Photoelectrochemical Water Splitting: Integration of Subsurface Dipoles with Atomic-Scale Control. *Advanced Energy Materials* **2016**, *6* (7), 1502154. https://doi.org/10.1002/aenm.201502154.

(47) Sankannavar, R.; Sarkar, A. The Electrocatalysis of Oxygen Evolution Reaction on $La_{1-x}Ca_xFeO_{3-\delta}$ Perovskites in Alkaline Solution. *International Journal of Hydrogen Energy* **2018**, *43* (9), 4682–4690. https://doi.org/10.1016/j.ijhydene.2017.08.092.

(48) Mohamed, R.; Cheng, X.; Fabbri, E.; Levecque, P.; Kötz, R.; Conrad, O.; Schmidt, T. J. Electrocatalysis of Perovskites: The Influence of Carbon on the Oxygen Evolution Activity. *Journal of The Electrochemical Society* **2015**, *162* (6), F579. https://doi.org/10.1149/2.0861506jes.

(49) Zhu, Y.; Zhou, W.; Shao, Z. Perovskite/Carbon Composites: Applications in Oxygen Electrocatalysis. *Small* **2017**, *13* (12), 1603793. https://doi.org/10.1002/smll.201603793.

Supporting Information

Revealing the intrinsic oxygen evolution reaction activity of perovskite oxides across conductivity ranges using thin film model systems

Lisa Heymann[†,*], Iris C. G. van den Bosch[§], Daan Wielens[§], Ole Kurbjeweit[†], Emma van der Minne[§], Ellen M. Kiens[§], Anton Kaus[†], Daniel Schön[†], Stephan Menzel[†], Bernard Boukamp[§], Felix Gunkel[†,*], Christoph Baeumer[†,§,*]

[†]Peter Gruenberg Institute 7, Forschungszentrum Juelich GmbH, 52428 Juelich, Germany and JARA-FIT, RWTH Aachen University, 52056 Aachen, Germany

[§]MESA+ Institute for Nanotechnology, Faculty of Science and Technology, University of Twente, Enschede, Netherlands

*Corresponding authors

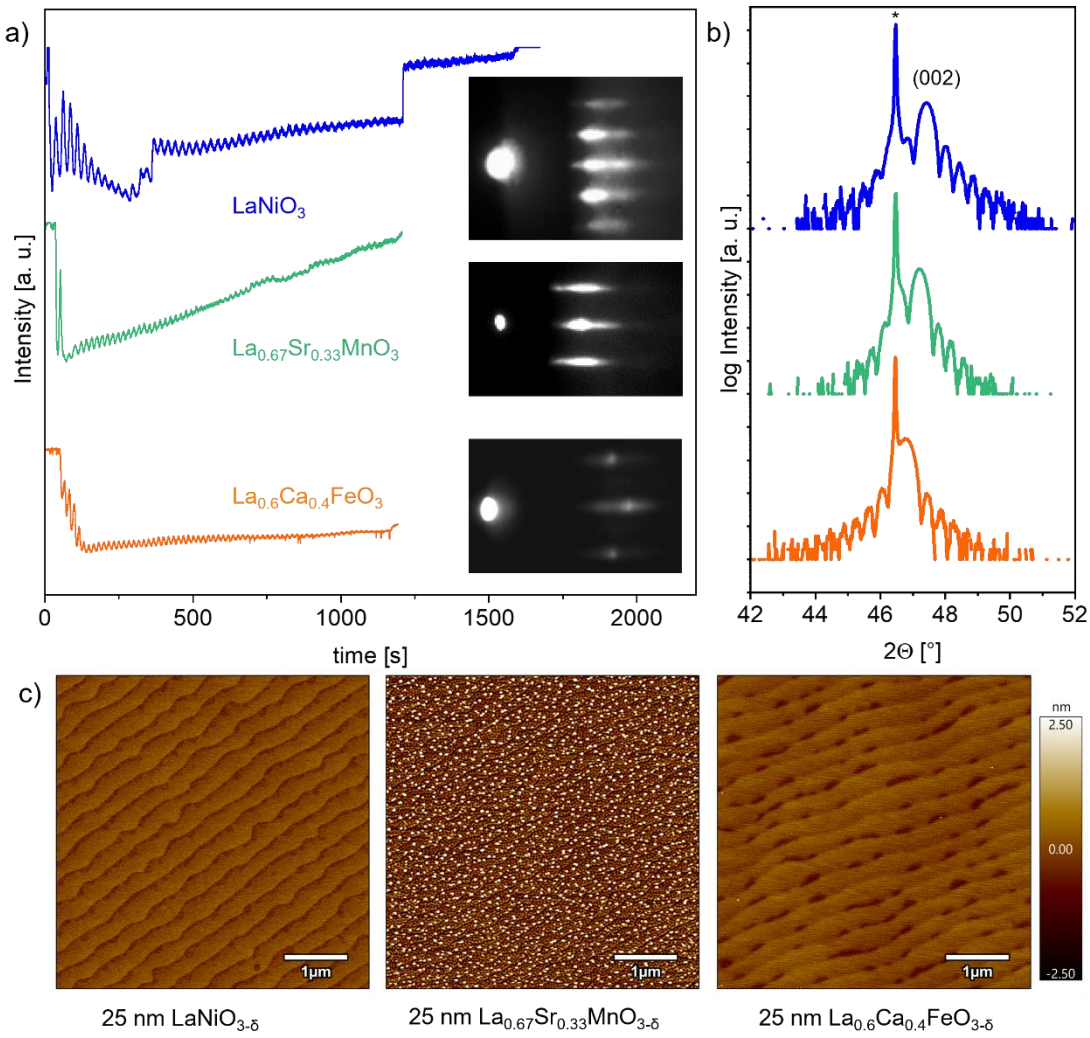

Figure S1: **a**) RHEED intensity oscillations of the specular spot for 25 nm thick $LaNiO_{3-\delta}$, $La_{0.67}Sr_{0.33}MnO_{3-\delta}$ and $La_{0.6}Ca_{0.4}FeO_{3-\delta}$ thin films deposited on $SrTiO_3$. The thin films grow in a layer-by-layer mode where in the case of $La_{0.67}Sr_{0.33}MnO_{3-\delta}$ and $La_{0.6}Ca_{0.4}FeO_{3-\delta}$, the RHEED oscillations start to fade out after 800 s. The sharp intensity increase seen for the $LaNiO_{3-\delta}$ growth stems from manually increased primary beam intensity at around 360 s and 1210 s. The corresponding RHEED patterns are shown on the right after 25 nm thin film growth. Insets: RHEED diffraction pattern. **b**) X-ray diffraction patterns of the corresponding thin films in 2θ-ω geometry. The peak marked with the * represents the diffraction signal of (002) $SrTiO_3$. The diffractograms were obtained after electrochemical treatment, confirming the high crystalline quality throughout the application. **c**) AFM scans of the corresponding thin films. $LaNiO_{3-\delta}$ and $La_{0.6}Ca_{0.4}FeO_{3-\delta}$ exhibit smooth, step-terraced morphology. The $La_{0.67}Sr_{0.33}MnO_{3-\delta}$ surface exhibits small islands of 7 nm height on top of the step-terraces. We find that the islands do not have major impact on the electrocatalytic properties by comparison to thinner films which do not exhibit such islands[1,2].

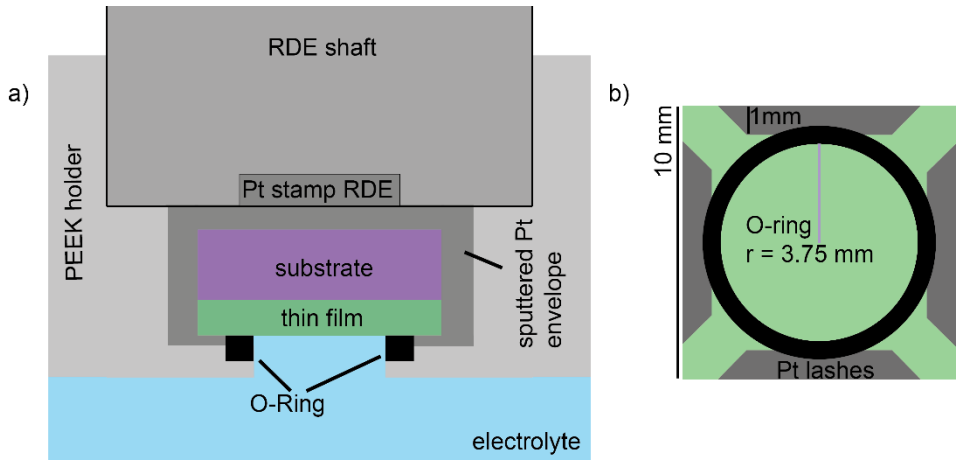

Figure S2: **a**) Sketch of a thin film mounted in the PEEK holder onto the RDE shaft. O-Ring seals the electrolyte from the sample backside and edges. The thin film is sputtered with 50 nm Pt to ensure electrical contact to the Pt stamp of the RDE. **b**) Sample geometry for electrochemical measurements. The width of sputtered Pt is 1 mm at the front edges. The sample area that is exposed to the electrolyte corresponds to the inner diameter of the O-ring (0.44 cm^2).

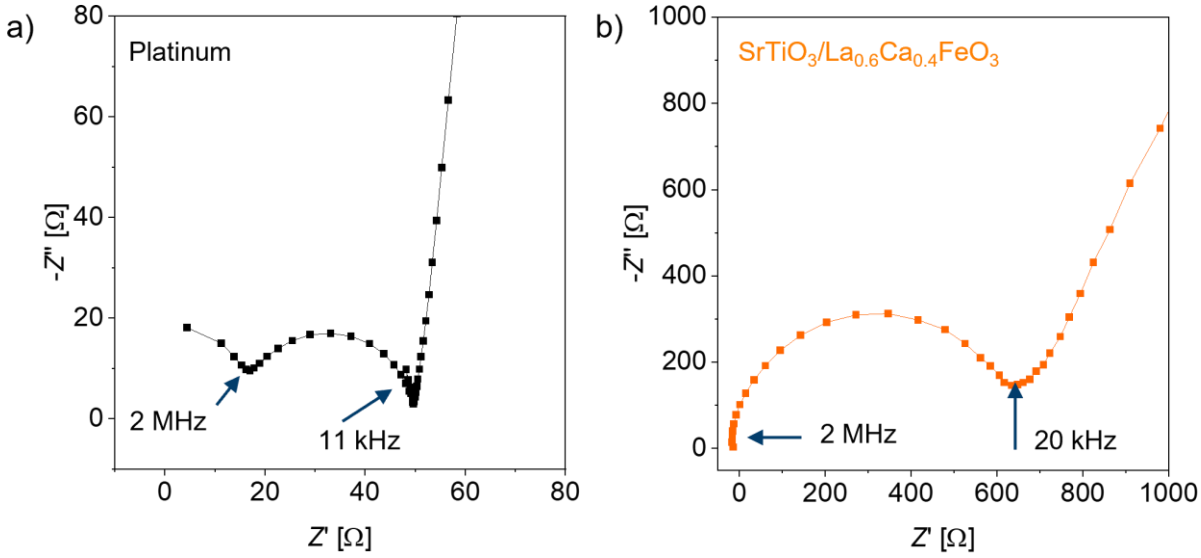

Figure S3: **a**) Nyquist plot of a Pt sample in the high frequency range. The sample was placed in 0.1 M KOH and the impedance was measured at open circuit voltage. There is a semicircle observed between 2 MHz and 11 kHz. When the reference electrode is equipped with a shunt that consists of a Pt wire and capacitor in parallel, the impedance feature systematically changes with capacitor size. Hence, the impedance feature can be attributed to the frit of the reference electrode, as was also described in the literature[3]. At 11 kHz, the imaginary part of the impedance is zero and the x-axis offset represents the uncompensated resistance R_u. At lower frequencies, a large incline is seen which is attributed to the working electrode solid/liquid interface. **b**) Nyquist plot of 25 nm $La_{0.6}Ca_{0.4}FeO_{3-\delta}$ on $SrTiO_3$ in the high frequency range. The impedance signal from the reference electrode (dominating at high frequencies) overlaps with the impedance signal of the working electrode and therefore -Z'' does not reach zero. This hinders an accurate determination of the R_u.

a)

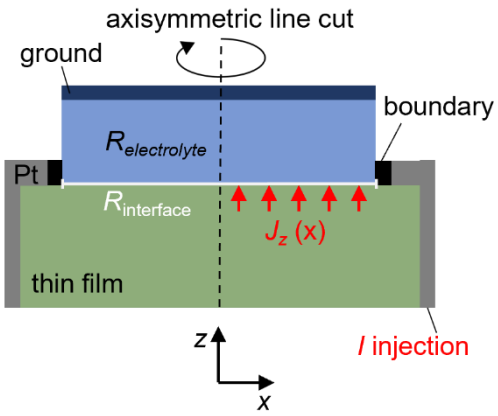

b)

Input parameters	Value/ equation
d(thin film)	25 nm
ρ(thin film)	According to fig. 1a manuscript
σ(thin film)	1/*ρ*
w(thin film)	5 mm
d(electrolyte)	10 µm
w(electrolyte)	3.75 mm
R(electrolyte)	50 Ω
σ(electrolyte)	$d_{electrolyte}/(\pi w_{\mathrm{electrolyte}}{}^2 * R_{\mathrm{electrolyte}})$
d(interface)	5 nm
R(interface)	100 Ω
σ(interface)	$d_{\mathrm{interface}}/(\pi w_{\mathrm{electrolyte}}{}^2 * R_{\mathrm{interface}})$
σ(Pt)	0.94x 10^7 S/m

c)

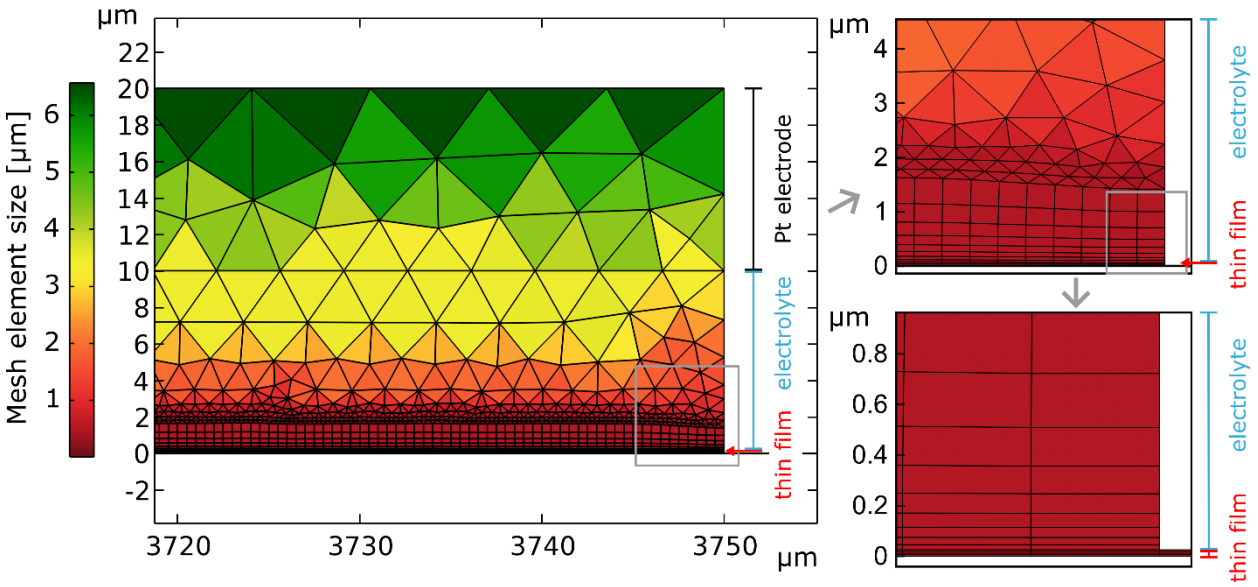

Figure S4: **a**) Sketch of the sample system geometry applied in the COMSOL study. The dashed line and circular arrow represent the axisymmetric line cut. The normal current density J_z was obtained below the sample surface in *x* direction from the sample center to the catalyst boundary (i.e. the O-ring). The electrolyte (blue box) is defined as a solid material with the resistance $R_{\mathrm{electrolyte}}$ = 50 Ω that is typically observed as uncompensated resistance (R_u) in our experiments (mainly stemming from the electrolyte resistance in 0.1 M KOH solution). The thin film/electrolyte interface resistance ($R_{\mathrm{interface}}$ = 100 Ω), i.e. the charge transfer resistance, is applied as a boundary condition directly at the interface and is marked with the white line. Above the electrolyte layer, the ground contact (as Pt electrode) is located. **b**) Summarized simulation parameters for thicknesses (*d*), widths (*w*), resistivity (*ρ*) and conductivity (*σ*).

c) Illustration of the 2D mesh. As the model has a very large width (5000°µm), but is very thin (20°µm), the mesh can only be visualized here using a section. Triangular and quadrilateral mesh elements are used. A comparatively large mesh can be utilized for the electrode and the electrolyte. Since the resistive film is very thin (0.025°µm), the mesh elements in the electrolyte are shrunk in the direction of the interface of the thin film. The top right graph is the zoom of the marked area in grey in the main panel. The graph in the bottom right is the zoom towards the thin film/electrolyte interface.

Simulation details

The current continuity equation $-\nabla\,\sigma\,\nabla\,\mathrm{V} = 0$ is solved in the electrolyte and thin film domain. σ is the conductivity and V is the potential. The whole Pt domain on top of the electrolyte is set to GND ($V = 0$), while the Pt side electrode serves as current source fulfilling

$$\oint \mathbf{nJ}\, dS = I_0,$$

where S is the surface of the domain, J is the current density and **n** the normal unit vector pointing outwards. I_0 is the applied current. All outer boundaries are considered insulating using a Neumann condition, i.e., $\mathbf{nJ} = 0$. At the interface between electrolyte and thin film, a thin interfacial resistive layer is assumed which is modeled using the boundary condition

$$\mathbf{nJ}_{\text{electrolyte}} = \frac{\sigma_{\text{interface}}}{d_{\text{interface}} * (V_{\text{electrolyte}} - V_{\text{thin film}})}$$

and

$$\mathbf{nJ}_{\text{thin film}} = \frac{\sigma_{\text{interface}}}{d_{\text{interface}} * (V_{\text{thin film}} - V_{\text{electrolyte}})}$$

Here, $d_{\text{interface}}$ is the virtual thickness of the interfacial layer and $\sigma_{\text{interface}}$ is the interface conductivity, which is calculated according to

$$\sigma_{\text{interface}} = \frac{d}{R_{\text{interface}}\ \pi\, r^2_{\text{electrolyte}}}$$

to result in a surface resistance of $R_{\text{interface}} = 100\ \Omega$. The voltages $V_{\text{thin film}}$ and $V_{\text{electrolyte}}$ are the local potentials along the interface within the thin film and the electrolyte, respectively. This condition leads to a potential jump at the thin film/electrolyte interface.

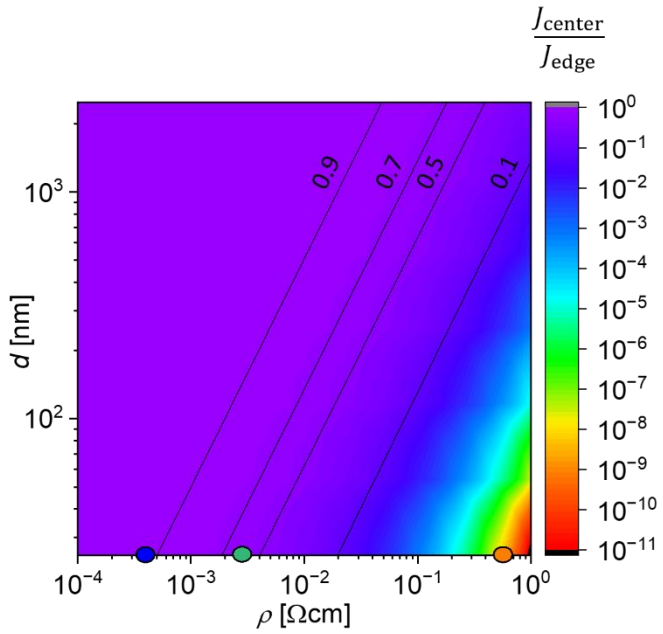

Figure S5: Heatmap of the $\frac{J_{center}}{J_{edge}}$ ratio on a logarithmic scale to obtain the rapidly increasing inhomogeneity above a resistivity of 2 10^{-2} Ωcm.

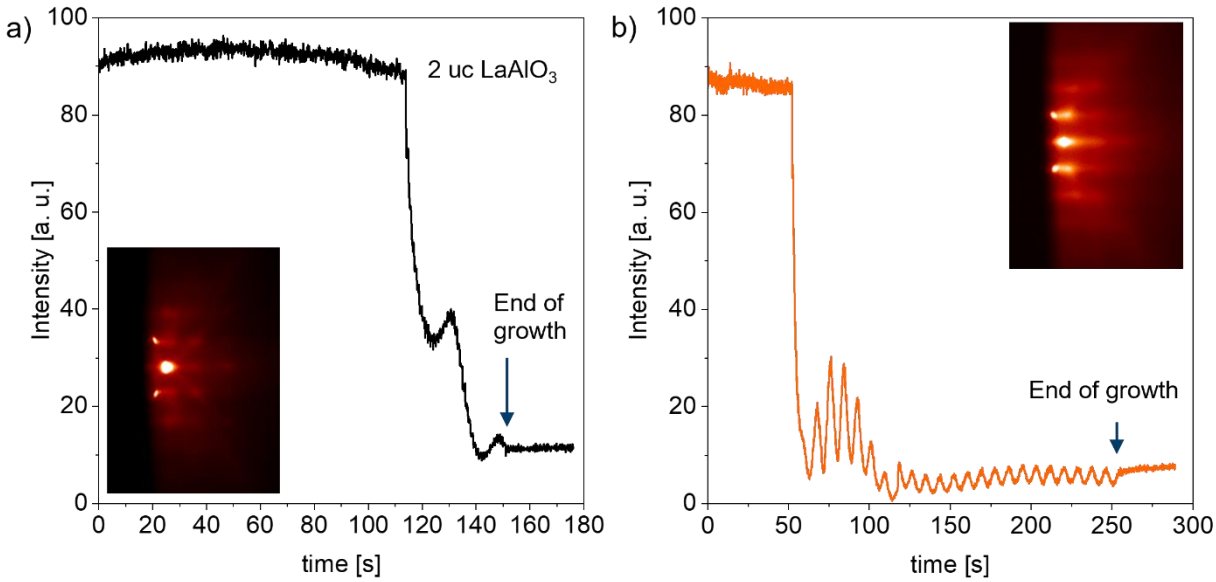

Figure S6: **a)** The growth of 2 uc $LaAlO_3$ on Nb:$SrTiO_3$. Inset: Initial RHEED pattern of the pristine substrate surface. The growth was stopped right after the second local maximum of the RHEED oscillation. **b**) Subsequent deposition of 25 uc of $LaNiO_3$ on the $LaAlO_3$ layer. Inset: Final RHEED pattern of the Nb:$SrTiO_3$/ $LaAlO_3$ 2 uc/ $LaNiO_3$ 25 uc stack, confirming high-quality growth with similar surface compared to Figure S1a).